Engineering Structures

Coupled Aero-Hydro-Geotech Real-Time Hybrid Simulation of Offshore Wind Turbine Monopile Structures

--Manuscript Draft--

Manuscript Number:	ENGSTRUCT-D-23-02123R2
Article Type:	VSI: Wind Turbine Structures
Keywords:	Renewable Energy; Offshore wind turbines; Real-time hybrid simulation; offshore wind turbine foundations; Soil-foundation-structure interaction; aerodynamic loading; hydrodynamic loading
Corresponding Author:	Safwan Al-Subaihawi, PhD Lehigh University Bethlehem , PA UNITED STATES
First Author:	Safwan Al-Subaihawi
Order of Authors:	Safwan Al-Subaihawi
	James Ricles
	Qasim Abu-Kassab
	Muhannad Suleiman
	Richard Sause
	Thomas Marullo
Manuscript Region of Origin:	North America
Abstract:	Real-time hybrid simulation (RTHS) divides a structural system into an analytical and experimental substructure. The former is based on a well-established analytical model while the latter consists of a physical model in the laboratory, for which there is not a well-established analytical model. This paper extends real-time hybrid simulation to monopile-type Offshore Wind Turbines (OWTs) to enable the investigation of their behavior considering the response of pile foundations under operational and more severe conditions. The embedded foundation and surrounding soil of the OWT are modeled physically in a soil box in the laboratory while the remaining parts of the system and loading are modeled analytically. The program OpenFAST, developed by the National Renewable Energy Laboratory (NREL), is linked to the RTHS coordinator to determine the hydrodynamic and aerodynamic loads acting on the OWT, along with modeling the dynamics of the electric power generation equipment and associated controller for the OWT. The RTHS framework along with its initial implementation and validation are described in this paper. RTHSs of a 5 MW OWT subjected to operational and more severe conditions are performed to experimentally validate the framework. The framework offers a realistic approach to investigate the behavior OWT structures supported on monopiles. This approach accounts for the coupled response of the OWT structure with is foundation, while experimentally capturing the nonlinearities of the soil-foundation interaction in real-time.
Suggested Reviewers:	Joel Conte, PhD Professor, University of California San Francisco jpconte@ucsd.edu Published in this field.
	Billie Spencer, PhD Professor, University of Illinois Urbana-Champaign bfs@illinois.edu Published in this field.
Opposed Reviewers:	
Response to Reviewers:	

Coupled Aero-Hydro-Geotech Real-Time Hybrid Simulation of Offshore Wind Turbine Monopile Structures

Safwan Al-Subaihawi [a], James Ricles [b], Qasim Abu-Kassab [c], Muhannad Suleiman [d], Richard Sause [e], Thomas Marullo [f]

[a] Corresponding author, Postdoctoral Research Associate, Department of Civil and Environmental Engineering, Lehigh University, 117 ATLSS Dr, Bethlehem, PA 18015, United States, E-mail: swa313@lehigh.edu, ORCID: 0000-0002-7876-5738

[b] Bruce G. Johnston Professor, Department of Civil and Environmental Engineering, Lehigh University, 117 ATLSS Dr, Bethlehem, PA 18015, United States, E-mail: jmr5@lehigh.edu, ORCID: 0000-0002-1545-5898

[c] Ph.D. Student, Department of Civil and Environmental Engineering, Lehigh University, 117 ATLSS Dr, Bethlehem, PA 18015, United States, E-mail: qaa219@lehigh.edu

[d] Professor of Geotechnical Engineering, Department of Civil and Environmental Engineering, Lehigh University, 117 ATLSS Dr, Bethlehem, PA 18015, United States, E-mail: mts210@lehigh.edu

[e] Joseph T. Stuart Professor of Structural Engineering, Department of Civil and Environmental Engineering, Lehigh University, 117 ATLSS Dr, Bethlehem, PA 18015, United States, E-mail: rs0c@lehigh.edu

[f] Research Scientist, ATLSS Engineering Research Center, Lehigh University, 117 ATLSS Dr, Bethlehem, PA 18015, United States, E-mail: tmm3@lehigh.edu

ABSTRACT

Real-time hybrid simulation (RTHS) divides a structural system into an analytical and experimental substructure. The former is based on a well-established analytical model while the latter consists of a physical model in the laboratory, for which there is not a well-established analytical model. This paper extends real-time hybrid simulation to monopile-type Offshore Wind Turbines (OWTs) to enable the investigation of their behavior considering the response of pile foundations under operational and more severe conditions. The embedded foundation and surrounding soil of the OWT are modeled physically in a soil box in the laboratory while the remaining parts of the system and loading are modeled analytically. The program OpenFAST, developed by the National Renewable Energy Laboratory (NREL), is linked to the RTHS coordinator to determine the hydrodynamic and aerodynamic loads acting on the OWT, along with modeling the dynamics of the electric power generation equipment and associated controller for the OWT. The RTHS framework along with its initial implementation and validation are described in this paper. RTHSs of a 5 MW OWT subjected to operational and more severe conditions are performed to experimentally validate the framework. The framework offers a realistic approach to investigate the behavior OWT structures supported on monopiles. This approach accounts for the coupled response of the OWT structure with its foundation, while experimentally capturing the nonlinearities of the soil-foundation interaction in real-time.

KEYWORDS

Renewable energy, offshore wind turbines, real-time hybrid simulation, offshore wind turbine foundations, soil-foundation-structure interaction, aerodynamic loading, hydrodynamic loading.

1. INTRODUCTION

Real-time hybrid simulation (RTHS) is a testing technique where the system is divided into analytical and experimental substructures [1, 2]. The former uses well-established computation

models to create a numerical model of a portion of the system. The remaining components of the system, for which there is no existing well-established computational model, is modeled physically in the laboratory. The two substructures are kinematically coupled and equilibrium is maintained at their common degrees of freedom (DOFs).

RTHS has historically been used to investigate the dynamic response of onshore structures to wind and earthquake loading. The prior RTHS studies included 40-story tall steel braced-frame buildings with viscous-damped outrigger systems [3-5], a 2-story reinforced concrete structure with moment resisting frames [6], 3-story steel building with moment resisting frames and braced frames with nonlinear viscous dampers [7- 9], 3-story steel building with moment resisting frames and braced frames with elastomeric dampers [10, 11], 3-story steel braced frame building with magnetorheological dampers [12, 13], and 3-story steel moment resisting frame building with floor isolation systems [14]. Currently, there is a considerable interest to increase the production of electricity from OWTs, with U.S federal mandates stipulating an increase of production to 30 GW by 2030 and 110 GW by 2050 [15, 16]. The size of the components of an OWT precludes testing a complete system in the laboratory and research on OWTs has been primarily limited to investigating the behavior of individual components [17-20]. Knowledge is limited on the behavior of the complete system including its foundation support system when subjected to operational and more severe loading conditions such as storms. The RTHS concept is extended in this paper to investigate the piled foundation behavior of monopile OWTs. RTHS will enable a complete OWT structure and its foundation system to be studied under various loading conditions, where the OWT and the associated externally applied aerodynamic and hydrodynamic loads are modeled analytically while the pile foundation is modeled experimentally inside a soil box as shown in Figure 1. For a given time step *i*, an integration algorithm determines the displacement and

velocities of the system, the experimental restoring forces are measured, the analytical substructure restoring forces computed, and the hydrodynamic and aero-elastic forces are obtained, enabling the explicit integration algorithm to complete the integration for the time step by solving for the acceleration. The coupling between the OWT model and the pile foundation is enforced at the mudline level.

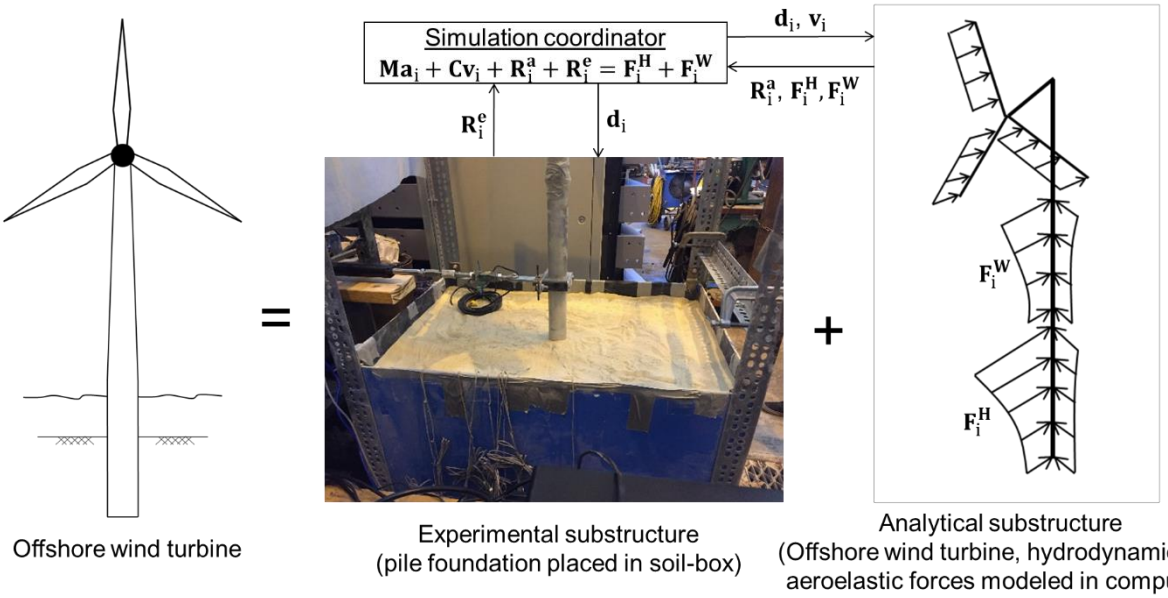

Figure 1: Generalized schematic of the real-time hybrid simulation concept for offshore wind turbines.

The short and long-term behavior of the pile foundation can be captured in a more realistic manner using the RTHS approach compared to subjecting the pile foundation to a predefined cyclic load or displacement (e.g., Frick and Achmus [21], Cox et al. [22], and Su et al. [23]). Furthermore, the soil profile corresponding to different geographical locations can be replicated in the soil box, and thus the behavior of the OWT supported on pile foundation under operational or more severe conditions corresponding to specific soil profiles can be captured in a RTHS.

Hybrid testing in ocean structures was initially proposed for deep water mooring systems by Buchner et al. [24]. The experimental substructure included the mooring segment near the water surface to avoid constructing deep and expensive basin tanks when testing such systems. The

implementation of RTHS to study floating offshore and onshore wind turbines (FOWTs) has been the subject of several recent studies published in the literature. Chabaud et al. [25] and Sun et al. [26] proposed a RTHS framework to study FOWTs where the floating device was envisioned to be modeled physically in the laboratory and the wind turbine including the blades, rotor, and tower are modeled analytically. Sadraddin and Shao [27] proposed using a geographically distributed RTHS framework to test FOWTs where the RTHS components are distributed among multiple laboratories, such as placing the turbine in a wind tunnel while the floating device is placed in a wave basin facility. The measured response quantities needed to perform the RTHS such as load cell readings are transferred to the simulation coordinator via a high-speed network. The above three FOWTs studies are conceptual in nature and the authors did not perform any experiments to prove the concept. Song et al. [28] proposed a RTHS framework for fixed-bottom OWTs where the blade-rotor assembly and aerodynamic loads are modeled analytically while the tower are envisioned to be modeled physically. However, like the other above-mentioned studies, this study is analytical in nature and the proposed framework has not yet been validated experimentally.

Several RTHS studies of FOWTs involving experimental work appear in the literature. Chabaud et al. [29], Thys et al. [30], Kanner et al. [31], Vilsen et al. [32], and Vittori et al. [33] performed RTHS of floating OWTs where the floating device in addition to the OWT tower were modeled experimentally at a reduced scale and placed in a wave basin, while the remaining OWT components including the blades and rotor along with the aerodynamic loads were modeled analytically. Bayati et al. [34] and Belloli et al. [35] performed RTHS testing of FOWTs where the blades, rotor, and tower were modeled physically at reduced scale in a wind tunnel, and the floating platform including the hydrodynamic loads were modeled analytically.

The RTHS of fixed-bottom OWTs is limited, and no RTHS have considered the Soil-Foundation-Structure Interaction (SFSI) effects. This paper addresses this knowledge gap , for it is the first experimental study that expands RTHS to fixed-bottom OWTs that includes the SFSI. The study uses OpenFAST to model the aerodynamic and hydrodynamic loading for the RTHS, where all OpenFAST modeling capabilities are preserved when integrating it into the RTHS framework presented in this paper. OpenFAST is an open-source software that is regularly maintained by the National Research Energy Laboratory (NREL), and has been experimentally and analytically validated by several researchers (Jonkman and Musial [36]; Bergua et al. [37]; Popko et al. [38]; Shaler et al. [39]).

It is important for the analytical substructure of a RTHS to accurately represent the part of the system that is modeled analytically. Although OpenFAST has the ability to model the SFSI effects, it uses models consisting of simplified linear springs located at the mudline. This approach is inappropriate to model the nonlinear SFSI coupled behavior of OWTs because linear springs are unable to capture the hysteric damping and nonlinear deformations that develop in the soil [40]. In addition, the formulation implemented in Sub-Dyn (a module in OpenFAST) to capture the dynamics of the submerged portion of an OWT is incompatible with the architecture for performing a RTHS. The formulation used by Sub-Dyn consist of a state space model based on the Craig-Bampton substructuring method [41] that is valid only for linear systems [42]. The current work developed a simulation coordinator to replace Sub-Dyn, and is interfaced to the pile foundation in the laboratory and to the aerodynamic and hydrodynamic modules in OpenFAST.

This paper presents the details of the RTHS framework, including aspects of the simulation coordinator, the interface of the simulation coordinator with OpenFAST, and the integration of the equations of motion. The implementation is demonstrated by performing a series of RTHS of a 5

MW OWT supported on a monopile subjected to operational and more severe conditions. In the RTHS, the pile foundation is modeled experimentally and the remaining parts of the structure are modelled analytically. A list of the main parameters and their values that appear throughout the paper are summarized in Table A.1 of Appendix A.

2. PROTOTYPE OFFSHORE WIND TURBINE DESCRIPTION

The 5 MW reference OWT model used in this study was developed by NREL [43]. The OWT has three glass-fiber blades with a rotor radius of 63m and hub height of 90m, and the blades are pre-bent to increase clearance and alleviate the risk of striking the tower. The tower is composed of a tapered circular steel section starting from a diameter of 6m and thickness of 0.027m at the base to a diameter of 3.87m and thickness of 0.019m at the top of the tower, where the base of the nacelle is located. The tower is connected to a 66m long circular steel monopile having a diameter of 6m and a wall thickness of 0.06m [44]. The monopile is divided into three segments: 10m above the water level, 20m submerged in the water, and 36m embedded in the soil below the mudline. The location where the tower of the OWT is connected to the monopile is called the transition piece.

The OWT drivetrain includes a multi-stage gearbox with a ratio of 97:1 and a rated rotor and generator speeds of 12 rpm and 1174 rpm, respectively. The cut-in and cut-off wind speeds of the OWT are 3 m/sec and 25m/sec, respectively. Additional details of the OWT are found in [43, 44]. The 1^{st} natural frequency of the OWT with foundation compliance included in models developed by Jonkman et al. [43,44] is reported to be about 0.25Hz and the highest frequency equal to about 3.0Hz.

3. REAL-TIME HYBRID SIMULATION CONFIGURATION

Figure 2 shows the configuration of an OWT installed on a monopile driven below the seabed. OpenFAST is used in the RTHS to model components above the transition piece and their dynamics that include the blades, tower, electric power generator, gearbox, rotor, drivetrain, nacelle, along with the externally applied aerodynamic and hydrodynamic loads as depicted in Figure 2. The model for the RTHS is shown in Figure 2(b)) and consists of four substructures: (1) tower-blades substructure; (2) transition substructure; (3) analytical substructure; and (4) experimental substructure. The tower-blades substructure models the tower and blades above the transition piece and is created using OpenFAST. The details of OpenFAST are presented later. The transition substructure models the transition piece. A transition node is defined at the intersection between the tower-blades and transition substructure that is shared among these two substructures. In addition, an interface node is defined at the intersection of the transition and analytical substructures, and is shared among these two substructures. The analytical substructure models the monopile below the transition piece and consists of several nodes (labeled analytical substructure nodes in Figure 2(b)). The experimental substructure, which models the monopile below the mudline, has a single node called the experimental substructure node that is located at the intersection with the analytical substructure. The transition substructure spans between the transition and interface nodes while the analytical substructure spans between the interface and the experimental substructure nodes (see Figure 2(b)). The vector of displacements ($\boldsymbol{d}$), velocities ($\boldsymbol{v}$), and accelerations ($\boldsymbol{a}$) at the transition node, ($\boldsymbol{d^T}$, $\boldsymbol{v^T}$, $\boldsymbol{a^T}$), interface node ($\boldsymbol{d^I}$, $\boldsymbol{v^I}$, $\boldsymbol{a^I}$), monopile analytical substructure nodes ($\boldsymbol{d^A}$, $\boldsymbol{v^A}$, $\boldsymbol{a^A}$), and the experimental substructure node ($\boldsymbol{d^E}$, $\boldsymbol{v^E}$, $\boldsymbol{a^E}$) are identified in Figure 2.

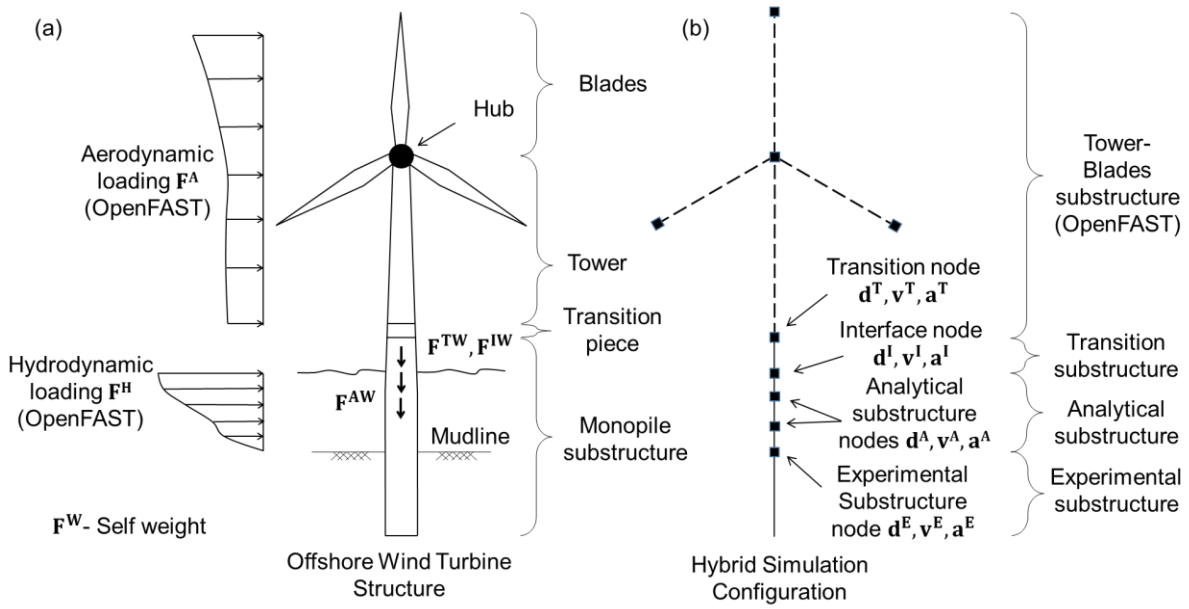

Figure 2: Real-time hybrid simulation configuration: (a) offshore wind turbine structure; (b) model hybrid simulation configuration.

The equations of motion of the OWT are given in Equation (1). Equation (1) represents dynamic equilibrium of the structure expressed at the DOF of the transition node, interface node, analytical substructure nodes, and experimental node. The equations of motion are shown partitioned with respect to the DOF of these nodes, and discussed later. OpenFAST provides the motions of the transition node ($\boldsymbol{d^T}, \boldsymbol{v^T}, \boldsymbol{a^T}$) associated with the dynamic response of all of the OWT components above the transition node that includes the effects of aerodynamic forces acting on the blades and tower, dynamics of the electric power generator, gearbox, rotor, drivetrain, nacelle and the associated control system for these components. OpenFAST also provides the hydrodynamic loads acting over the height of the OWT (i.e., the transition substructure and analytical substructure) that is submerged beneath the still water surface. $\boldsymbol{F^{TH}}$, $\boldsymbol{F^{IH}}$, $\boldsymbol{F^{AH}}$, and $\boldsymbol{F^{EH}}$ in Equation (1) are the vector of hydrodynamic forces that act at the transition node, interface node, analytical substructure nodes, and the experimental substructure node, respectively. $\boldsymbol{F^{TW}}$, $\boldsymbol{F^{IW}}$, $\boldsymbol{F^{AW}}$, and $\boldsymbol{F^{EW}}$ in Equation (1) are vectors of gravity loads based on the self-weight of the structure acting on the transition node, interface node, analytical substructure nodes, and the experimental

substructure node, respectively. $\boldsymbol{F^{TA}}$ in Equation (1) is the vector of forces at the transition node that are in dynamic equilibrium with the aerodynamic loads acting on the tower and blades of the OWT, along with the forces associated with the dynamics of the electric power generator, gearbox, rotor, drivetrain, nacelle and the associated control system for these components. The mass matrix $\boldsymbol{M}$, inherent damping matrix $\boldsymbol{C}$, stiffness matrix $\boldsymbol{K}$, along with the remaining submatrices that appear in Equation (1) are discussed later.

$$\underbrace{\begin{bmatrix} m_T & 0 & 0 & 0 \\ 0 & & & \\ 0 & & \boldsymbol{M} & \\ 0 & & & \end{bmatrix}\begin{Bmatrix} a^T \\ a^I \\ a^A \\ a^E \end{Bmatrix}}_{\text{Mass}} + \underbrace{\begin{bmatrix} c_T & 0 & 0 & 0 \\ 0 & & & \\ 0 & & \boldsymbol{C} & \\ 0 & & & \end{bmatrix}\begin{Bmatrix} v^T \\ v^I \\ v^A \\ v^E \end{Bmatrix}}_{\text{Damping}} + \underbrace{\begin{bmatrix} k_{TT} & k_{TI} & 0 & 0 \\ k_{IT} & & & \\ 0 & & \boldsymbol{K} & \\ 0 & & & \end{bmatrix}\begin{Bmatrix} d^T \\ d^I \\ d^A \\ d^E \end{Bmatrix}}_{\text{Stiffness}} = \underbrace{\begin{Bmatrix} F^{TH} + F^{TW} + F^{TA} \\ F^{IH} + F^{IW} \\ F^{AH} + F^{AW} \\ F^{EH} + F^{EW} \end{Bmatrix}}_{\text{Applied loads}} \quad (1)$$

4. MODELING OF HYDRODYNAMIC, AEROELASTIC, AND OWT POWER GENERATION EQUIPMENT LOADS

The hydrodynamic, aeroelastic, and OWT power generation equipment load effects were modeled using OpenFAST. OpenFAST is an open-source tool developed by NREL to model onshore and offshore wind turbines subjected to operational and non-operational environmental conditions. This paper uses OpenFAST version 3.1.0. The OWT components are modeled using several modules of OpenFAST that are shown in Figure 3. The environmental conditions that account for aerodynamic, ice, and hydrodynamic loadings are computed in the Inflow-Wind, Ice-Dyn, and Hydro-Dyn modules, respectively. The external aeroelastic and hydrodynamic loads acting on the OWT are computed in Aero-Dyn and Hydro-Dyn, respectively, while the OWT dynamics are computed in Elasto-Dyn/Beam-Dyn and Servo-Dyn. OpenFAST users can create a high-fidelity model of the OWT blades using the Beam-Dyn module. The drivetrain, nacelle, and tower dynamics are modeled in Elasto-Dyn. The dynamics created from the power generation equipment and OWT controllers is modeled in Servo-Dyn. The Ice-Dyn module was not used in the RTHS. The RTHS coordinator and the interface with the OpenFAST modules, including the outputs of Elasto-Dyn, Aero-Dyn, and Hydro-Dyn is discussed in Section 9 and shown in Figures 7 and 8.

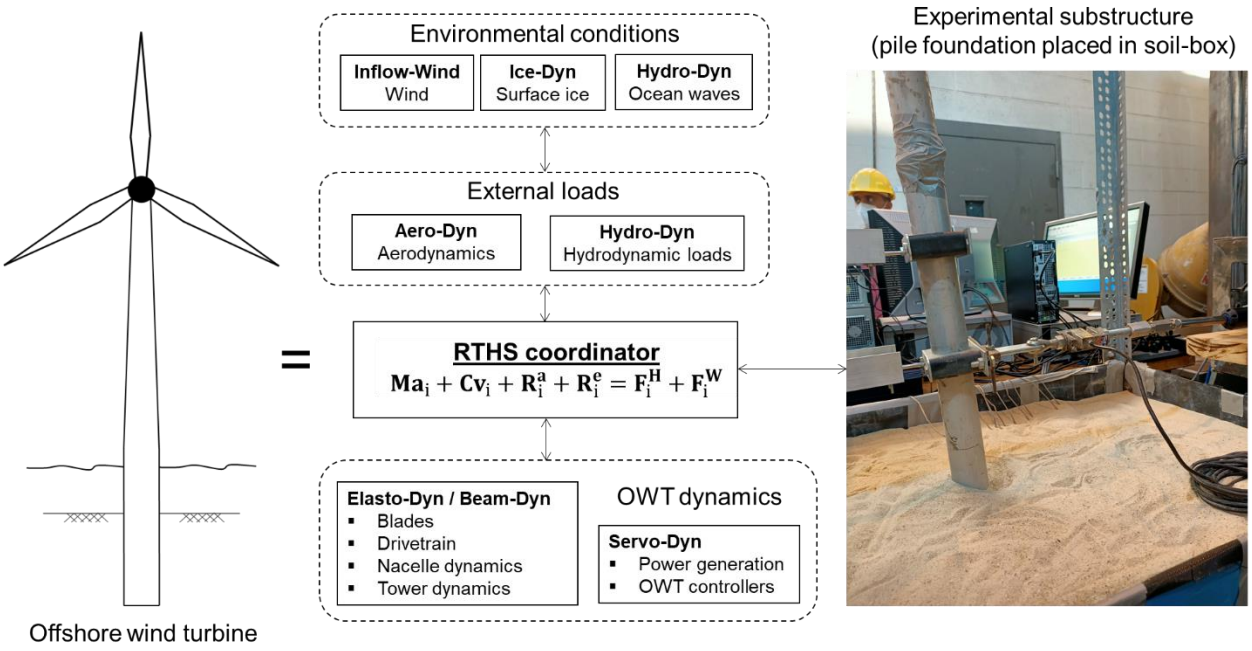

Figure 3: Schematic of OpenFAST modules and RTHS coordinator.

The structural dynamics of the OWT tower and blades are computed by the OpenFAST module called Elasto-Dyn. Each blade is discretized into 17 elements and the models of the blades and tower are based on 6th order polynomial mode shapes and member properties recommended by Jonkman et al. [43]. Actuator lines are used to approximate the three-dimensional flow of the fluid around the tower and blades [45]. This approximation results in two-dimensional distributed loads that are integrated into three-dimensional loads. Aero-Dyn, an OpenFAST module linked to Elasto-Dyn, computes the aerodynamic loads based on Blade Element Momentum Theory (BEMT) after receiving the nodal displacements and velocities of the blade and the freestream velocity of the fluid from OpenFAST [45]. The relationship between the angle of attack of the blade, uplift and drag forces, and the pitching moment are defined in OpenFAST input file based on the blade geometry and therefore used directly to estimate nodal forces. The Beddoes-Leishman unsteady aerodynamics model [46] is applied to the BEMT solution to account for flow hysteresis [45]. The losses near the blade's tip and root are accounted for when obtaining the aerodynamic

forces acting along the blade. Further details regarding the tower-blades substructure modeling in OpenFAST can be found in [45, 47]. All modes of vibration of the blades are assigned a modal damping ratio of 0.47% by OpenFAST. The tower modes of vibration are assigned a higher modal damping ratio of 1% as suggested by Jonkman et al. [43]. Additional details regarding the description of the 5MW-OWT model are given in [43].

The hydrodynamic loads acting on the monopile are calculated using the Hydro-Dyn module in OpenFAST [48]. The monopile hydrodynamic loads can be modeled in this module using either the potential-flow or strip theory. In this study the monopile hydrodynamic loads were modeled using strip-theory because the diameter of the monopile is small relative to the wavelength [45]. Strip-theory uses Morison's equation [49], where the monopile flexibility is considered when applying Morison's equation and therefore the hydrodynamic forces depend on the relative acceleration and velocity between the fluid and the submerged structure [45]. Morison's equation consists of viscous drag (F_D), fluid inertia (F_{MI}), and added hydrodynamic mass (F_{AM}) forces per unit length acting on a submerged member [48, 50]:

$$F_M = F_D + F_{MI} + F_{AM} = \frac{1}{2}\rho C_d D v_r |v_r| + C_M \frac{\pi}{4}\rho D^2 a_f - (C_M - 1)\frac{\pi}{4}\rho D^2 a_s \quad (2)$$

where ρ is the water density, C_d is the drag coefficient, D is the member's diameter, v_r is the relative velocity between the fluid particle velocity v_f and structural velocity v_s, C_M is the inertia coefficient, a_s is the structural acceleration, and a_f is the fluid particle acceleration. Morison's equation is appropriate when the member diameter-to-wave length ratio $\frac{D}{\lambda} < 0.05$ (Bai and Bai [51]). For the 20m water depth, which is considered an intermediate depth, and with a wavelength λ ~121m and wave period of T = 10 sec. used in this study, $\frac{D}{\lambda} = 0.03$ at the water surface where the maximum fluid velocity and acceleration exist.

Wave elevations are generated by Hydro-Dyn with the assumption that the wave is regular and possesses no stretching (i.e., wave kinematics are computed between the seabed and mean sea water level). The hydrodynamic coefficients for C_d and C_M are given in [44], where values of C_d = 1.0 and C_M = 2 are used in this paper, and no marine growth is assumed.

Elasto-Dyn models the dynamics of the nacelle, rotor, and drivetrain and is coupled to Aero-Dyn and Servo-Dyn, where the latter models the power generation equipment and the associated control system. The drivetrain between the hub and the electric generator is modeled as an axially rigid torsional spring acting in parallel with a dashpot. The stiffness and dashpot constants are 867MN.m/rad and 6.2MN.m/(rad/sec), respectively, representing the equivalent stiffness and damping of the gearbox and speed shafts. The electric generator efficiency is taken as 94.4% with an inertia of 534tons.m^2 about the high-speed shaft. The relative motion between the nacelle and the yaw actuator was accounted for in the OpenFAST model by including a linear rotational spring and dashpot with constants of 9GN.m/rad and 19MN.m/(rad/sec), respectively. Hub translation and rotational inertia are 56tons and 115tons.m^2, respectively. The nacelle translational and rotational masses are 240tons and 2,607tons.m^2, respectively. The 5MW-OWT included generator-torque and blade-pitch logical controllers within the Servo-Dyn module in OpenFAST. These controllers regulate power generation and the generator speed. The generator-torque controller in OpenFAST included several control regions. The first region is before the minimum generator speed of 670 rpm at which the generator's torque is zero. The last region is after the rated generator speed of 1173.7 rpm, where the controller aims at maintaining constant generator power. The blade-pitch controller aims at regulating the generator speed in this last region. The blade-pitch rate limit is set to 8 degree/sec according to Jonkman et al. [43]. The OWT

electric generator is modeled in OpenFAST using the Thevenin Equivalent Circuit. As noted previously, additional details regarding the description of the 5MW-OWT model are given in [43].

The OpenFAST calculations and the RTHS integration of the equations of motion are performed at full-scale.

5. TRANSITION AND ANALYTICAL SUBSTRUCTURES

The monopile segment above the water (namely, the transition substructure) is 10m long and modeled using a single 3D element. The analytical substructure of the RTHS is comprised of the segment of the monopile below the transition substructure and is submerged beneath the mean water surface (only the analytical substructure is submerged in this study). The submerged 20m long monopile is modeled with 8 equal length 3D linear beam-column elements. A consistent mass formulation of the elements of the analytical substructure is used and adapted from Damiani et al. [42]. The transition substructure uses a lumped mass formation to simplify the coupling of the equations of motion shown in Equation (1). The stiffness properties of the elements of the transition and analytical substructures are based on Damiani et al. [42].

6. EXPERIMENTAL SUBSTRUCTURE

The experimental substructure for the RTHS consists of an available 1/120 scale circular aluminum pile embedded in dry loose sand placed in the soil box shown in Figure 4. Due to the availability of existing test specimens for the experimental substructure, it was assumed that the pile for the full-scale structure was also aluminum material. A schematic of the test setup for the experimental substructure is shown in Figure 4(c). The pile represents the portion of the monopile that is embedded into the seafloor below the mudline. The pile has a 0.05m diameter, 2mm thickness, and an embedment length of 0.6m. This embedment length was selected to accommodate the soil box dimensions and is longer than that corresponding to the 1/120 scale factor. The lateral

resistance of the foundation is primarily in the direction of the hydrodynamic and aerodynamic loading loads. In the RTHS, only the lateral DOF is incorporated into the experimental substructure. Three of the remaining DOFs of the experimental substructure node have their restoring forces computed numerically, while two DOF (axial and twist) are restrained. In future studies, actuators will be used to impose motions to all six DOF and provide a complete set of experimental restoring forces. This task will require accounting for actuator kinematics and coupling effects which is beyond the scope of the current study.

As shown in Figure 4(c), one actuator is used in the current study to impose the target lateral displacement onto the pile during a RTHS. The actuator is an electric actuator manufactured by UltraMotion (model A1 Series) with a force capacity of 0.45kN and a stroke limit of 0.08m. The actuator is anchored to a reaction frame consisting of a W10x39 steel column. A 2.2 kN load cell manufactured by ARTECH (model 20210-500) is inserted between the clevis and the actuator to measure the restoring force R_i^e developed by the experimental substructure at time step *i* caused by the lateral displacement d_i^E imposed by the actuator. R_i^e is used by the simulation coordinator to integrate the equations of motion at time step *i*, and will be discussed later. The instrumentation included the load cell in addition to an LVDT to measure the pile position and strain gages placed along the pile. The instrumentation was connected to a data acquisition system (DAQ). The LVDT had a 200-mm stroke and was manufactured by Duncan Electronics.

The sand in the soil box has a density of 1630kg/m^3 and internal friction angle of 35 degrees. The RTHS in this paper used a scale factor of where $\alpha = 120$, where the target displacement for the pile from the full-scale simulation is scaled down by a factor of 1/ α, to match the small-scale pile. This scaling law is based on structural model testing involving dynamic loading effects, where the basic quantities of mass, length, and time describe the dynamics problem

with the acceleration of gravity preserved in the reduced and full-scale models [52]. In geotechnical testing, the measured restoring force is scaled up by a factor of $N\alpha^2$, where N = model mean stress-to-prototype mean stress ratio [53]. In the RTHS a value of N=1 was used. It is important to emphasize that the purpose of this paper is to present a RTHS framework that captures the short- and long-term behavior of the OWT pile foundation using RTHS, and it is not intended to critique the behavior of a specific small-scale pile foundation. The scaling law and the geometry of the pile used in this paper may need further refinement to enforce similitude and this additional work is outside the scope of the current study. The time axis is not scaled when performing the RTHS in this paper because of the following reasons: 1) the time scale factor is $1/\sqrt{\alpha} = 1/10.95$ and OpenFAST is unable to perform the state determination of the OWT at 10.95 times faster than real-time; 2) the soil box is filled with dry sand and the rate of loading does not significantly affect its behavior during a RTHS [54-56]; 3) the small integration time step needed to run the simulation in real-time when scaling the time axis is smaller than what can be accommodated by the clock sampling rate of the actuator's controller, which is 1/1024 sec. It is envisioned that adoptees of the RTHS framework presented herein will use larger scale pile specimens, whereby the compressed time axis in the simulations is compatible with OpenFAST and the actuator's controller clock speed.

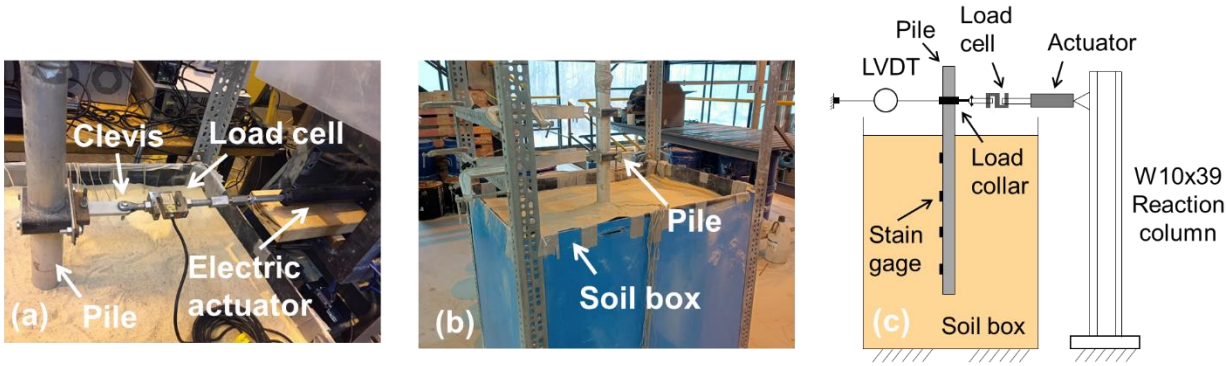

Figure 4: Experimental substructure for real-time hybrid simulation: a) pile-actuator interface; b) pile shown embedded in soil box; and, (c) schematic of test setup and instrumentation.

7. RTHS INTEGRATED CONTROL ARCHITECTURE

The RTHS integrated control architecture is depicted in Figure 5. It includes a simulations computer, xPC target computer, data acquisition (labeled DAQ), and SCRAMNet. SCRAMNet provides communication between the computers at a speed of 90ns to enable data sharing. xPC refers to a real-time Speedgoat system with a real-time operating system. The xPC target computer operates using the xPC Target real-time operating system developed by Mathworks [57]. It enables one to compile Simulink models [57] with a C-compiler to execute real time simulations. The xPC, which runs at a clock speed of 400Hz, operates a serial controller to control the actuator position and logs the actuator load cell readings used by the RTHS coordinator for the integration process (the RTHS coordinator is discussed in Section 8) and the pile's position for actuator compensation to minimize actuator delay and amplitude errors. The simulation computer is a Dell workstation equipped with the Windows operating system that hosts the tower-blades substructure in OpenFAST and the RTHS coordinator where the remaining substructure models reside. The Dell computer was equipped with an Intel i-9 processor and 32 gigabytes of random-access memory. The data acquisition system (labeled DAQ in Figure 5) records the load cell reading, the LVDT position sensor that measures the position of the pile during the RTHS, and strain gauges that are placed on the pile embedded in the soil. A 180 Watt power supply manufactured by UltraMotion (model P/N: PS-1X0A) was used to provide electric power to the actuator.

The RTHS coordinator integrates the equations of motion and sends the target actuator command from the simulation computer over SCRAMNet to the xPC. The xPC has a programmed closed loop PID control, where it issues the command displacement to the actuator and receives the feedback of the measured extension or contraction of the actuator. The actuator position is measured by the actuator's internal transducer and communicated to the xPC via a direct I/O

connection. The xPC sends the restoring force of the pile (measured using the load cell) to the simulation computer over SCRAMNet. The xPC and simulation computer are synchronized (discussed later) and exchange data every 1/1024sec. The data acquisition system scans at the rate of 4096Hz and records the data at a rate of 1024Hz. A copy of the DAQ recorded data is transferred to the xPC and then over SCRAMNet back to the simulation computer.

A communication delay exists and is associated with the xPC's clock speed of 400Hz for issuing commands to the actuator and recording feedback data from the DAQ. Consequently, the communication delay between the simulation computer issuing an actuator command displacement is 1/400sec. while receiving the feedback signal of the load cell reading and measured actuator displacement is an additional 1/400sec., resulting in a total communication delay of 5msec for each time step of a RTHS. The RTHS integrated control architecture enables adaptive compensation for actuator control to account for delay. It was determined that a 5msec delay had minimal effect on a RTHS, and therefore actuator delay compensation was not used for the RTHS. Further discussion about this is presented later in this section of the paper and in Section 16 *Assessment of RTHS Results.*

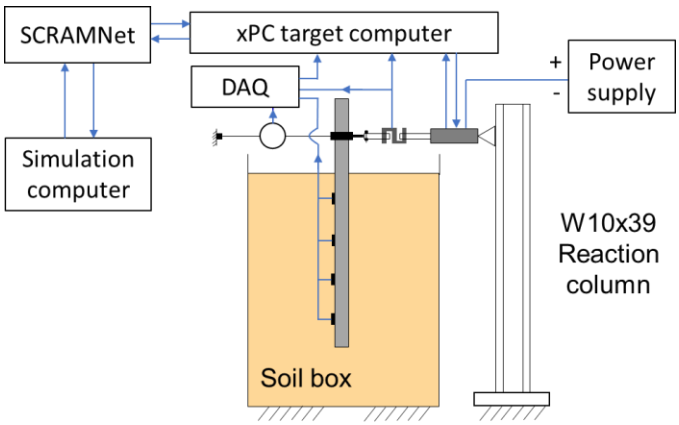

Figure 5: Integrated Control Architecture for RTHS.

The dynamic behavior of the transfer system was investigated over a range of frequencies. The transfer system of the test setup consisted of the components shown in Figure 5 and included the simulation computer, SCRAMNet, xPC, actuator controller, electric actuator, power supply, load cell, DAQ, LVDT feedback displacement transducer, W10x39 steel reaction column, and the experimental substructure. To assess the system dynamics using an analytical transfer function requires the linearization of the experimental substructure due to the nonlinear behavior of the force-deformation response of the pile embedded in the soil box. An analytical transfer function can only be obtained for linear and time invariant systems. Therefore, to assess the system dynamics of the RTHS setup the procedure recommended by Carrion and Spencer [58] was used to obtain the frequency response function (FRF) from the actuator command displacement to the measured displacement of the actuator obtained by the LVDT and fed back to the simulation coordinator. The excitation input consisted of band-limited white noise with a frequency range of 0 to 35Hz and an amplitude of 1.5mm, which was generated by the RTHS simulation coordinator residing on the simulation computer. The RMS value was based on the cyclic displacement amplitude developed in Test 1 of the RTHS (the RTHS results are to be presented in Section 15 *Hybrid Simulation Results*). Data was recorded at a rate of 400Hz over a 165sec. duration. The FRF was calculated using 66000 Fast Fourier Transform (FFT) points with a Hanning windowing with 50% overlap and 35 averages. The FRF of the system appears in Figure 6, where it is plotted up to 35Hz. The FRF has a magnitude near a unit value up to about 4.5 Hz, where an increase occurs due to a presence of a natural frequency in the transfer system in the range of 12 to 15Hz associated with resonance of the pile embedded in the soil box. This range of natural frequency is caused by the nonlinear behavior of the soil. The roll-off frequency is at 35 Hz (i.e., where a drop of 3 dB in magnitude occurs relative to the magnitude at 0Hz). The magnitude of the FRF is shown

plotted in Figure 6 over the frequency range of 0 to 3Hz, which is the range of frequencies associated with the OWT natural frequencies and the expected frequency range of response of the experimental substructure during a RTHS. The frequency decomposition of the experimental substructure motions during a RTHS are discussed later in Section 14 *RTHS Coordinator Assessment* and Section 15 *Hybrid Simulation Results.* Within the frequency range of 0 to 3Hz the FRF has a magnitude in the range of 0.993 to 1.063 with an average value of 1.020. The phase plot of the FRF was used to establish the time delay in the transfer system as a function of frequency, and is shown in Figure 6. It was determined that the time lag delay over the frequency range of 0 to 3Hz has an average of 5.4msec. A majority of the time lag delay of 5.4msec is due to the 5msec communication delay discussed previously. The results for the magnitude imply that no significant dynamics exist in the system over the frequency range of associated with the natural frequencies of the OWT.

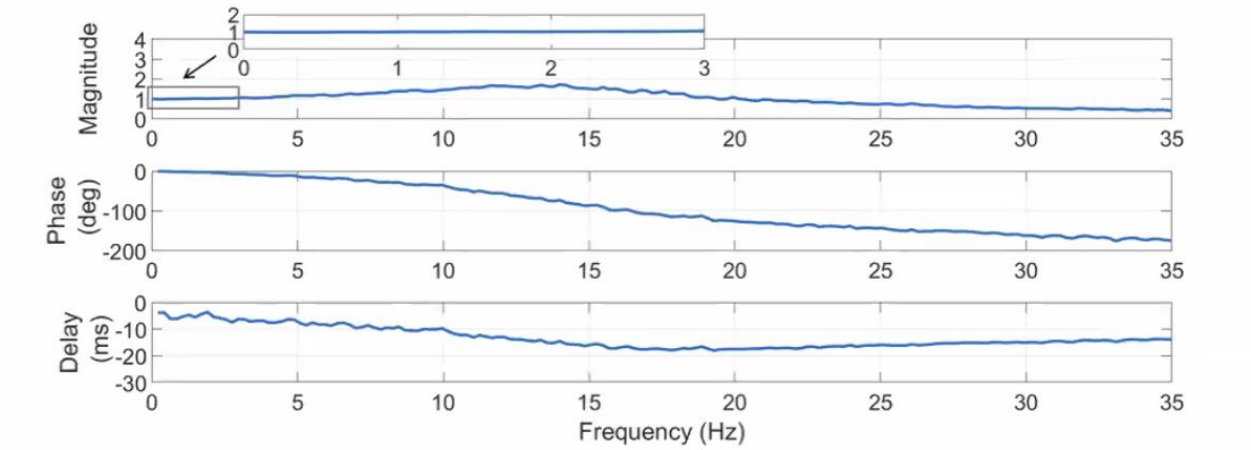

Figure 6: Transfer system frequency response function from actuator command displacement to measured displacement.

8. REAL-TIME HYBRID SIMULATION COORDINATOR

The simulation coordinator oversees the integration of the equations of motion. To integrate the equations of motion, it is necessary to partition the equations of motion as shown in Equation (1). This produces a force boundary condition at the interface node between the transition and

analytical substructures. The force $\boldsymbol{F}_i^I$ associated with this boundary condition is based on dynamic equilibrium at the end of the transition substructure element connected to the interface node, as described below in Section 9.1. The subset of the equations of motion associated with the DOFs of the interface node and the nodes of the analytical and experimental substructures correspond to the submatrices in the lower right partition of Equation (1) are integrated by including $\boldsymbol{F}_i^I$. Interfacing with the OpenFAST model above the transition node required establishing equilibrium and compatibility at the transition node, where OpenFAST provides the simulation coordinator a vector of trial set of displacements ($\boldsymbol{d}^T$), velocities ($\boldsymbol{v}^T$), and accelerations ($\boldsymbol{a}^T$) at the transition node associated with the aerodynamic effects acting on the blades and the tower and the dynamics of the electric power generator, gearbox, rotor, drivetrain, nacelle and the associated control system for these components. The equations of motion are related to the matrix elements in the upper part of the partitioned matrix and the loads applied to the transition node in Equation (1) are then solved in an iterative manner with a predictor-corrector method to satisfy equilibrium and compatibility at the transition node. The predictor-corrector procedure in OpenFAST [45] involves the following three steps for each iteration for a given time step [59]: (1) predict the state of the tower above the transition piece at the end of the current time step; (2) pass this information to the monopile substructure and calculate the predicted response of this substructure at the end of the current time step; (3) correct the calculated state of the tower above the transition piece at the end of the current time step. Steps (2) and (3) can be specified by the user to be repeated to improve the solution to the equations of motion at the end of the given time step. This is the iteration process described later. In Step (1) the estimate of the state (displacements, velocities, accelerations, and restoring forces) at the end of the current time step is based on extrapolating the state at the beginning of the current step using the forward finite difference. In Step (2), the Craig-Bampton method [41] is

used to integrate the equations of motion to obtain the response of the monopile substructure below the transition piece. In Step (3), the state of the tower above the transition piece is the corrected using the Adams-Bashforth-Moulton (ABM) method [60,61] to integrate the equations of motion associated with the OWT tower model above the transition node. In any subsequent iterations for the current time step the ABM results from Step (3) are used in Step (2).

The Adams-Bashforth-Moulton (ABM) method to integrate the equations of motions associated with the OWT tower model above and at the transition node is performed by Elasto-Dyn. This integration method is conditionally stable, where a numerical instability may occur if the integration time step is too large [59]. The stability of the Elasto-Dyn numerical integration process is heavily influenced by the modal characteristics of the transition substructure. For the selected transition substructure properties with a length of 10m it was found that an integration time step of Δt = 3/1024 sec. was adequate. If the length of the transition substructure is reduced from 10m to 3.3m the maximum stable integration time step is reduced from 3/1024 sec. to 1/1024 sec. (see [59] for further details on the effect of transition substructure stiffness on OpenFAST numerical instabilities).

As noted above, OpenFAST calculates the hydrodynamic loads acting on the analytical substructure using Morison's equation. Integration of the subset of equations of motion is performed in an explicit manner where the structural velocities are known at the beginning of the time step. Hence, the hydrodynamic loading can be readily determined without iterating within the time step. The inertia related hydrodynamic loading was considered by placing the hydrodynamic mass on the left-hand side of the equations of motion in the mass matrix $\boldsymbol{M}$ associated with the degrees of freedom of the analytical substructure and the interface node, see Equation (1), where it is treated as added mass.

9. INTEGRATION OF THE EQUATIONS OF MOTION

The equations of motion for a RTHS are expressed using restoring forces of the analytical and experimental substructures and can be written in the following general form:

$$\boldsymbol{M}\boldsymbol{a}_i + \boldsymbol{C}\boldsymbol{v}_i + \boldsymbol{R}^{\boldsymbol{a}}(\boldsymbol{d}_i^A, \boldsymbol{v}_i^A) + \boldsymbol{R}_i^e = \boldsymbol{F}_i \tag{3}$$

where $\boldsymbol{M}$ and $\boldsymbol{C}$ are the analytically modeled mass and damping matrices of the system, respectively; $\boldsymbol{R}^{\boldsymbol{a}}(\boldsymbol{d}_i^A, \boldsymbol{v}_i^A)$ and $\boldsymbol{R}_i^e$ are the analytically determined and experimentally measured restoring force vectors, respectively, at time step *i*, and $\boldsymbol{d}_i$, $\boldsymbol{v}_i$, $\boldsymbol{a}_i$, and $\boldsymbol{F}_i$ are the displacement, velocity, acceleration, and the excitation force vectors, respectively, at time step *i.* The $\boldsymbol{M}$ and $\boldsymbol{C}$ need to be formulated considering that the inertia and damping effects of the experimental substructure are taken into account through $\boldsymbol{R}^{\boldsymbol{e}}$. In addition, as implied in Equation (3), $\boldsymbol{R}^{\boldsymbol{a}}$ may be a function of displacement and velocity (e.g., supplemental dampers that exist in the analytical substructure), where any velocity-dependent forces $\boldsymbol{R}^{\boldsymbol{a}}$ are excluded in the viscous damping forces affiliated with $\boldsymbol{C}$. Note that the added mass is included in $\boldsymbol{M}$, whereas the viscous drag and inertia of the fluid are included in $\boldsymbol{F}_i$.

The equations of motion are integrated using the dissipative unconditionally stable explicit model-based Modified KR-α (MKR-α) algorithm [62]. It is a parametrically dissipative integration algorithm with controlled numerical damping that assigns minimal damping to the lower modes of vibration [62]. The simulation coordinate performs the integration of the equations of motion associated with the DOF at the interface, substructure, and experimental nodes. The analytical, experimental, and transition substructures are connected to the simulation coordinator, as shown in Figure 7, and the simulation coordinator communicates with OpenFAST through the modules Elasto-Dyn and Hydro-Dyn. The integration of the equations of motion involves the use of the restoring forces from the analytical substructure, $\boldsymbol{R}_i^{\boldsymbol{a}}$, experimental substructure, $\boldsymbol{R}_i^{\boldsymbol{e}}$,

hydrodynamic loads, $\boldsymbol{F}_{i,j}^{H}$, constant self-weight nodal forces, $\boldsymbol{F}^{W}$, and the interface nodal forces, $\boldsymbol{F}_{i,j}^{I}$, of the transition substructure, respectively, where the latter is associated with the motions $\boldsymbol{d}_i^T, \boldsymbol{v}_i^T, \boldsymbol{a}_i^T$ and nodal force $\boldsymbol{F}_{i,j}^{TA}$ at the transition node. $\boldsymbol{d}_i^T, \boldsymbol{v}_i^T, \boldsymbol{a}_i^T$ and nodal force $\boldsymbol{F}_{i,j}^{TA}$ are determined in an iterative manner, where the iteration occurs over a specified number of iterations that is controlled by OpenFAST and set by the user to j_{max}.

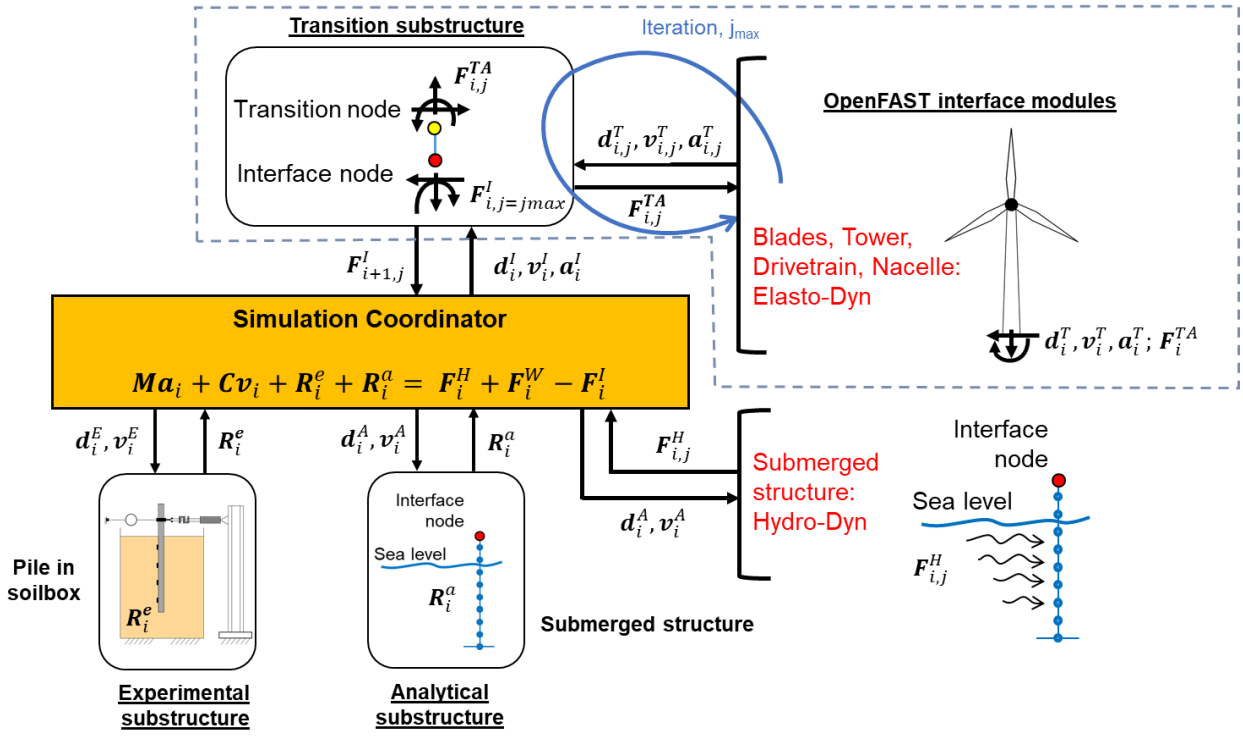

Figure 7: Real-time hybrid simulation configuration: interconnectivity of the simulation configuration with the analytical, substructure, and transition substructures and OpenFAST.

The displacement and velocity relations used in the MKR-α algorithm are:

$$\boldsymbol{d}_i = \left[\boldsymbol{d}_i^I\ \boldsymbol{d}_i^A\ \boldsymbol{d}_i^E\right]^T = \boldsymbol{d}_{i-1} + \Delta t \boldsymbol{v}_{i-1} + \left(\frac{1}{2}+\gamma\right)\Delta t \hat{\boldsymbol{v}}_{i-1}\,, \qquad \boldsymbol{v}_i = \left[\boldsymbol{v}_i^I\ \boldsymbol{v}_i^A\ \boldsymbol{v}_i^E\right]^T = \boldsymbol{v}_{i-1} + \hat{\boldsymbol{v}}_{i-1} \tag{4a, b}$$

where:

$$\hat{\boldsymbol{v}}_i = \boldsymbol{A}\left[\boldsymbol{F}_{i-\alpha_f} - \boldsymbol{F}_{ID_{i-\alpha_f}} - \boldsymbol{R}_{i-\alpha_f} - \hat{\boldsymbol{F}}_{I_{i-1}}\right],\ \ \boldsymbol{F}_{i-\alpha_f} = (1-\alpha_f)(\boldsymbol{F}_i) + \alpha_f(\boldsymbol{F}_{i-1}),$$

$$\boldsymbol{F}_{ID_{i-\alpha_f}} = \boldsymbol{C}^a\left[\boldsymbol{v}_{i-1} + (1-\alpha_f)\hat{\boldsymbol{v}}_{i-1}\right],\ \ \boldsymbol{R}_{i-\alpha_f} = (1-\alpha_f)(\boldsymbol{R}_i^a + \boldsymbol{R}_i^e) + \alpha_f(\boldsymbol{R}_{i-1}^a + \boldsymbol{R}_{i-1}^e),\ \ \hat{\boldsymbol{F}}_{I_{i-1}} = \boldsymbol{B}\hat{\boldsymbol{v}}_{i-1} \tag{5a, b, c, d, e}$$

In Equation (4) the displacement vectors $\boldsymbol{d}_i^I, \boldsymbol{d}_i^A, \boldsymbol{d}_i^E$ and velocity vectors $\boldsymbol{v}_i^I, \boldsymbol{v}_i^A, \boldsymbol{v}_i^E$ were previously defined. The accelerations used in the MKR-α algorithm are obtained by satisfying dynamic equilibrium, whereby:

$$\boldsymbol{a}_i = \left[\boldsymbol{a}_i^I \; \boldsymbol{a}_i^A \; \boldsymbol{a}_i^E\right]^T = \boldsymbol{D}\hat{\boldsymbol{v}}_i \tag{6}$$

where the accelerations vectors $\boldsymbol{a}_i^I, \boldsymbol{a}_i^A, \boldsymbol{a}_i^E$ were also defined previously.

In Equation (5) $\boldsymbol{F}_{i-\alpha_f}, \boldsymbol{F}_{ID_{i-\alpha_f}}$ and $\boldsymbol{R}_{i-\alpha_f}$ are the weighted external load, weighted damping force, and weighted restoring force vectors, respectively, where $\boldsymbol{F}_i$ and $\boldsymbol{F}_{i-1}$ in Equation (5) are the loads applied to the system at time steps *i* and *i – 1*:

$$\boldsymbol{F}_i = \boldsymbol{F}_i^H + \boldsymbol{F}^W + \boldsymbol{F}_i^I, \quad \boldsymbol{F}_{i-1} = \boldsymbol{F}_{i-1}^H + \boldsymbol{F}^W + \boldsymbol{F}_{i-1}^I \tag{7a, b}$$

In Equation (7), $\boldsymbol{F}_i^H$ and $\boldsymbol{F}_{i-1}^H$ are the hydrodynamic nodal forces at time steps *i* and *i – 1*, respectively, $\boldsymbol{F}^W$ is the constant self-weight nodal forces, and $\boldsymbol{F}_i^I$ and $\boldsymbol{F}_{i-1}^I$ the interface nodal forces at time steps *i* and *i – 1*, respectively.

The matrices $\boldsymbol{A}$, $\boldsymbol{B}$, and $\boldsymbol{D}$ are defined by:

$$\boldsymbol{A} = \Delta t \boldsymbol{\alpha_1}[\boldsymbol{M} - \boldsymbol{M}\boldsymbol{\alpha_3}]^{-1}, \qquad \boldsymbol{B} = \frac{1}{\Delta t}\boldsymbol{M}\boldsymbol{\alpha_3}\,\boldsymbol{\alpha_1}^{-1}, \qquad \boldsymbol{D} = \frac{1}{\Delta t}\,\boldsymbol{\alpha_1}^{-1} \tag{8a, b, c}$$

$\boldsymbol{\alpha_1}$, $\boldsymbol{\alpha_2}$, $\boldsymbol{\alpha_3}$ are model-based integration parameters that are dependent on the model characteristics of the system and are calculated as:

$$\boldsymbol{\alpha_1} = \left[\boldsymbol{M} + \gamma\Delta t\widetilde{\boldsymbol{C}} + \beta\Delta t^2\boldsymbol{K}\right]^{-1}\boldsymbol{M}, \qquad \boldsymbol{\alpha_2} = \left(\frac{1}{2} + \gamma\right)\boldsymbol{\alpha_1},$$
$$\boldsymbol{\alpha_3} = \left[\boldsymbol{M} + \gamma\Delta t\widetilde{\boldsymbol{C}} + \beta\Delta t^2\boldsymbol{K}\right]^{-1}\left[\alpha_m\boldsymbol{M} + \alpha_f\gamma\Delta t\widetilde{\boldsymbol{C}} + \alpha_f\beta\Delta t^2\boldsymbol{K}\right] \tag{9a, b, c}$$

where:

$$\boldsymbol{C} = \boldsymbol{C}^a + \boldsymbol{C}^e, \quad \widetilde{\boldsymbol{C}} = \boldsymbol{C} + \boldsymbol{C}^v, \quad \boldsymbol{K} = \boldsymbol{K}^a + \boldsymbol{K}^e, \quad \boldsymbol{M} = \boldsymbol{M}^a + \boldsymbol{M}^e \tag{10a, b, c, d}$$

The matrices $\boldsymbol{M}$ and $\boldsymbol{K}$ above are the mass and stiffness matrices of the combined analytical and experimental substructures. The interface node is considered to be part of the analytical substructure in $\boldsymbol{M}$ and $\boldsymbol{K}$. The mass matrix $\boldsymbol{M}$ includes the mass associated with the self-

weight of the monopile and, as noted above, the added hydrodynamic mass lumped at the translational degrees of freedom. The lumped added hydrodynamic mass is based a value of $0.25(C_M - 1)\pi L D^2 \gamma_w / g$, where C_M is is the inertia coefficient (a value of 2.0 was used), L is the tributary length of the node associated with nodes of adjacent elements, D is the diameter of the monopile (equal to 6m), γ_w is the water unit weight (equal to 9.81kN/m^3), and g is the gravitational constant (9.81m/sec^2). The damping $\widetilde{\boldsymbol{C}}$, stiffness $\boldsymbol{K}$, and mass $\boldsymbol{M}$ matrices in Equation (9) are the sum of the contributions from the analytical (i.e., $\boldsymbol{C}^a$, $\boldsymbol{K}^a$, and $\boldsymbol{M}^a$) and experimental, (i.e., $\boldsymbol{C}^e$, $\boldsymbol{K}^e$, and $\boldsymbol{M}^e$) substructures, in addition to the hydrodynamic damping associated with viscous drag, $\boldsymbol{C}^v$, as shown in Equation (10b). These matrices are associated with the DOF at the interface, substructure, and experimental nodes, where:

$$\boldsymbol{M} = \begin{bmatrix} \boldsymbol{m}_{II} & \boldsymbol{m}_{IA} & 0 \\ \boldsymbol{m}_{AI} & \boldsymbol{m}_{AA} & \boldsymbol{m}_{AE} \\ 0 & \boldsymbol{m}_{EA} & \boldsymbol{m}_{EE} \end{bmatrix}, \quad \boldsymbol{K}^a = \begin{bmatrix} \boldsymbol{k}_{II} & \boldsymbol{k}_{IA} & 0 \\ \boldsymbol{k}_{AI} & \boldsymbol{k}_{AA} & \boldsymbol{k}_{AE} \\ 0 & \boldsymbol{k}_{EA} & \boldsymbol{k}^a_{EE} \end{bmatrix}, \quad \boldsymbol{K}^e = \begin{bmatrix} 0 & 0 & 0 \\ 0 & 0 & 0 \\ 0 & 0 & \boldsymbol{k}^e_{EE} \end{bmatrix} \tag{11}$$

$$\boldsymbol{C}^a = \begin{bmatrix} \boldsymbol{c}_{II} & \boldsymbol{c}_{IA} & 0 \\ \boldsymbol{c}_{AI} & \boldsymbol{c}_{AA} & \boldsymbol{c}_{AE} \\ 0 & \boldsymbol{c}_{EA} & \boldsymbol{c}^a_{EE} \end{bmatrix}, \quad \boldsymbol{C}^e = \begin{bmatrix} 0 & 0 & 0 \\ 0 & 0 & 0 \\ 0 & 0 & \boldsymbol{c}^e_{EE} \end{bmatrix}, \quad \boldsymbol{C}^v = \begin{bmatrix} \boldsymbol{c}^v_{II} & 0 & 0 \\ 0 & \boldsymbol{c}^v_{AA} & 0 \\ 0 & 0 & \boldsymbol{c}^v_{EE} \end{bmatrix} \tag{12}$$

$\widetilde{\boldsymbol{C}}$ is used only for the purposes of computing the integration parameters and therefore includes $\boldsymbol{C}^e$ and $\boldsymbol{C}^v$. The submatrix $\boldsymbol{c}^e_{EE}$ appearing in $\boldsymbol{C}^e$ is described below while $\boldsymbol{C}^v$ is discussed in Section 10.

The MKR-α algorithm is a one parameter algorithm associated with the high frequency spectral radius ρ_∞ [62]. ρ_∞ can be assigned any value in the range [1, 0] where values of ρ_∞ = 1 and 0 produce zero and maximum numerical damping, respectively. In this study, a value of $\rho_\infty = 0.75$ is used, which provides adequate high-frequency dissipation without affecting the lower-frequency modes of interest. The MKR-α algorithm has four model parameters α_m, α_f, β and γ which are related to the single free parameter ρ_∞,

$$\gamma = 0.5 - \alpha_m + \alpha_f, \quad \beta = 0.5(0.5 + \gamma), \quad \alpha_m = \frac{2\rho_\infty^3 + \rho_\infty^2 - 1}{\rho_\infty^3 + \rho_\infty^2 + \rho_\infty + 1}, \quad \alpha_f = \frac{\rho_\infty}{\rho_\infty + 1} \tag{13a, b, c, d}$$

OpenFAST assumes steady state loading conditions from the onset of an analysis, but assigns zero initial conditions (i.e., initial displacements velocities, and restoring forces) to the state of the structure. Under these conditions, an applied load at the start of an analysis is resisted by only the inertia forces of the system, causing an acceleration pulse. This is inappropriate for a RTHS because the sudden application of the loads and the ensuing acceleration pulse can lead to a significant displacement at the beginning of the simulation, which when applied to the experimental substructure can cause damage to the pile foundation and the surrounding soil. To alleviate this problem, Rayleigh mass and initial stiffness proportional damping with a 1% damping ratio for the first (0.25Hz) and last (3.0Hz) modes of the OWT is assigned to the analytical substructure. The Rayleigh damping is assigned based on the frequencies of the complete system (i.e., the OWT tower and the structure below the transition piece) and not the analytical substructure alone because the substructure will respond at the frequency of the complete system. Rayleigh damping is augmented with modal damping [40] assigned to all of the modes to suppress the response in the transient phase and alleviate unrealistic damage to the pile foundation and the soil, see Equation 14(a). This modal damping linearly diminishes over a duration of t_{Tr} in proportion to the time-dependent variable $\xi(t)$, where only the Rayleigh mass and stiffness proportional damping remains when the time t exceeds t_{Tr}:

$$\boldsymbol{C}^a = \begin{cases} \xi(t)\left(\boldsymbol{M}\left(\sum_{n=1}^{NDOF} \frac{2\omega_n}{M_n}\emptyset_n\emptyset_n^T\right)\boldsymbol{M}\right) + a_0\boldsymbol{M} + a_1\boldsymbol{K}^a, & t \le t_{Tr} \\ a_0\boldsymbol{M} + a_1\boldsymbol{K}^a, & t > t_{Tr} \end{cases}, \qquad (14a, b)$$

where $\xi(t) = \xi(0)(1 - t_i/t_{Tr})$. The modal damping ratio $\xi(t)$ is initialized to $\xi(0) = 0.2$ to create a highly damped system capable of suppressing the transient response and is decreased linearly to zero over the time duration of t_{Tr} = 120 sec. Numerical simulations in OpenFAST performed by the authors demonstrated that the steady state response is reached after 120 sec.

Upon reaching $t = t_{Tr}$ only Rayleigh proportional damping remains. An attribute of modal damping is that it enables specific damping values to be assigned to all of the modes of vibration. Rayleigh proportional damping does not have this attribute, justifying the choice of using modal damping to suppress the transition vibrations. In accordance with Equation (14a), all the modes of vibration are assigned the same modal damping ratio $\xi(t)$, where in this equation ω_n, M_n and $\emptyset_n$, are the frequency, modal mass, and the mode shape for the n^{th} mode of vibration, and $n \in [1, \text{NDOF}]$, where NDOF is the total number of degrees of freedom and therefore modes of the system (consisting of the analytical and experimental substructures). The total stiffness of the substructure $\boldsymbol{K}$ is used when determining the mode shapes that appear in Equation 14(a) to account for foundation compliance.

The model integration parameters $\boldsymbol{\alpha_1}, \boldsymbol{\alpha_2}, \boldsymbol{\alpha_3}$ in Equations (9a, b, c) are divided into the two groups $(*)_O$ and $(*)_U$, where $(*)_O$ are the parameters based on the damping during the transient phase defined by $\boldsymbol{C}^a$ using Equation (14a) at $\xi(0)$, while $(*)_U$ is based on the damping during the steady state phase defined by $\boldsymbol{C}^a$ using Equation (14b). These model integration parameters need to be calculated only once at the start of a RTHS.

As noted previously, the pile in the soil box was controlled using only one actuator orientated in the horizontal direction as shown in Figure 4, while the flexibility of the pile foundation associated with the other degrees of freedom is analytically accounted for in the RTHS by using linear springs and dashpots. The stiffness of these springs is based on the geometry and soil profile of the 5MW-OWT model reported in Aasen et al. [63], where the stiffness matrix for the foundation node is uncoupled:

$$\boldsymbol{k}_{EE}^{e} = \begin{bmatrix} k_{eq}^{F}(\omega) & 0 & 0 & 0 \\ 0 & k_y & 0 & 0 \\ 0 & 0 & k_{\Theta x} & 0 \\ 0 & 0 & 0 & k_{\Theta y} \end{bmatrix} \tag{15}$$

In Equation (15) k_y, $k_{\Theta x}$, and $k_{\Theta y}$ are the analytical defined foundation stiffnesses where k_y= 2.5E+6kN/m and $k_{\Theta x} = k_{\Theta y}$=2.6E+8kN/rad. $k_{eq}^{F}\ (\omega)$ represents the equivalent stiffness of the pile foundation (i.e., the experimental substructure) at full scale used to determine the model-based integration parameters. During the RTHS, however, $k_{eq}^{F}\ (\omega)$ is discarded and the experimental measured restoring force that acts in the x-axis direction is used. Only translations and rotations about the two horizontal x- and y-axes are considered in $\boldsymbol{k}_{EE}^{e}$ because the stiffness values associated with the vertical translational DOF along the longitudinal axis (z-axis) of the pile and torsional rotation are restrained. Linear dashpots are placed in parallel with the springs with dashpot coefficients equal to $\boldsymbol{c}_{EE}^{e} = a_0\boldsymbol{k}_{EE}^{e}$, where a_0 is the same stiffness proportionality factor used in Equation (14). With the exception for the determination of the model-based integration parameters, the first element in $\boldsymbol{c}_{EE}^{e}$ associated with the x-axis velocity is taken to be zero. This is because the measured restoring force of the experimental substructure during a RTHS includes both the displacement and velocity-dependent forces. For the determination of the model-based integration parameters, the equivalent pile damping coefficient, $c_{eq}^{F}\ (\omega)$**,** is used to define the first element in $\boldsymbol{c}_{EE}^{e}$. Both $k_{eq}^{F}\ (\omega)$**,** $c_{eq}^{F}\ (\omega)$ are discussed later in Section 10.

9.1 RTHS RESPONSE DETERMINATION PROCEDURE

The algorithm to conduct a RTHS is shown in flow chart form in Figure 8, where each of the steps of the algorithm are described below. The algorithm involves initializing the OWT accelerations of the system, followed by the OWT response determination of the RTHS. At the beginning of each time step, the transition substructure has a trial set of displacements $\boldsymbol{d}_{i,j}^{T}$, velocities $\boldsymbol{v}_{i,j}^{T}$, and accelerations $\boldsymbol{a}_{i,j}^{T}$ imposed at the transition node from Elasto-Dyn associated with iteration j, while the simulation coordinator receives the applied hydrodynamic loads $\boldsymbol{F}_{i,j}^{H}$ from Hydro-Dyn and computes the corresponding displacements, velocities, and accelerations of the analytical and

experimental substructure DOFs, as depicted in Figure 7. The resulting restoring forces $\boldsymbol{F}_{i,j}^{\boldsymbol{TA}}$ at the transition node based on the motions of the transition and interface nodes that are in dynamic equilibrium with the hydrodynamic loads and self-weight loads applied to the transition node are passed back to Elasto-Dyn. Elasto-Dyn then updates the trial values for $\boldsymbol{d}_{i,j}^{T}$, $\boldsymbol{v}_{i,j}^{T}$, and $\boldsymbol{a}_{i,j}^{T}$ and another iteration cycle is repeated, as depicted in Figure 7. This iteration process is repeated in order to establish compatibility and equilibrium at the transition node between the OWT tower above the transition node modeled by OpenFAST and the transition substructure below the transition node. It was found that the RTHS performed in this study required a maximum of three iterations to achieve convergence.

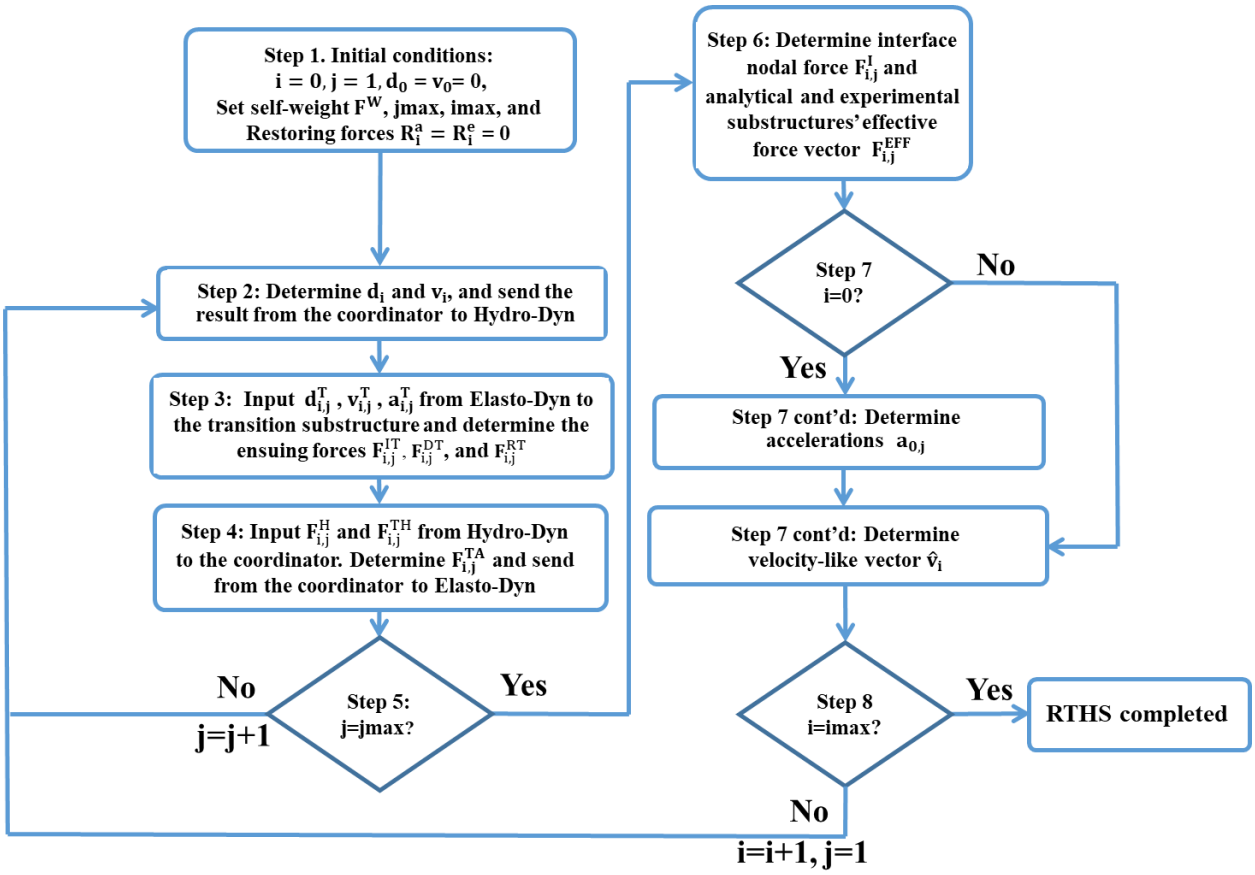

Figure 8: Flow chart for real-time hybrid simulation.

The response determination for a RTHS consists of the following eight steps:

Step 1. Set initial conditions, $i = 0$, where $t_i = i\Delta t, j = 1$, and $\boldsymbol{d}_i = \boldsymbol{v}_i = \boldsymbol{0}$

Step 2 If i = 0 then from Step 1 $\boldsymbol{d}_i = \boldsymbol{v}_i = \mathbf{0}$, otherwise determine the displacement and velocity of the substructure for the current integration time step:

$$\boldsymbol{d}_i = \left[\boldsymbol{d}_i^I \;\; \boldsymbol{d}_i^A \;\; \boldsymbol{d}_i^E\right]^T = \boldsymbol{d}_{i-1} + \Delta t \boldsymbol{v}_{i-1} + \left(\frac{1}{2} + \gamma\right)\Delta t \hat{\boldsymbol{v}}_{i-1} \tag{16}$$

$$\boldsymbol{v}_i = \left[\boldsymbol{v}_i^I \;\; \boldsymbol{v}_i^A \;\; \boldsymbol{v}_i^E\right]^T = \boldsymbol{v}_{i-1} + \hat{\boldsymbol{v}}_{i-1} \tag{17}$$

Send the result for $\boldsymbol{d}_i$ and $\boldsymbol{v}_i$ to Hydro-Dyn.

Step 3 Input $\boldsymbol{d}_{i,j}^T$, $\boldsymbol{v}_{i,j}^T$, $\boldsymbol{a}_{i,j}^T$ from Elasto-Dyn to the transition substructure. Compute the ensuing forces $\boldsymbol{F}_{i,j}^{IT}$, $\boldsymbol{F}_{i,j}^{DT}$, and $\boldsymbol{F}_{i,j}^{RT}$, where

$$\boldsymbol{F}_{i,j}^{IT} = \boldsymbol{m}_T \boldsymbol{a}_{i,j}^T, \qquad \boldsymbol{F}_{i,j}^{DT} = \boldsymbol{c}_T \boldsymbol{v}_{i,j}^T, \qquad \boldsymbol{F}_{i,j}^{RT} = [\boldsymbol{k}_{TT} \; \boldsymbol{k}_{TI}] \begin{pmatrix} \boldsymbol{d}_{i,j}^T \\ \boldsymbol{d}_i^I \end{pmatrix} \tag{18a, b, c}$$

The vector $\boldsymbol{d}_i^I$ is the displacement of the interface node, and equal to zero for $i = 0$ and $j \in (1, j_{max})$ because the interface node is part of the analytical substructure that starts from an initially undeformed position with zero initial velocity. The matrices $\boldsymbol{m}_T$, $\boldsymbol{c}_T$, $\boldsymbol{k}_{TT}$, and $\boldsymbol{k}_{TI}$ are submatrices of the mass $\boldsymbol{m}^{TI}$, damping $\boldsymbol{c}^{TI}$, and stiffness $\boldsymbol{k}^{TI}$ matrices of the beam-column element of the transition substructure connecting the transition and interface nodes, see Figure 2, where:

$$\boldsymbol{m}^{TI} = \begin{bmatrix} \boldsymbol{m}_T & 0 \\ 0 & \boldsymbol{m}_{II} \end{bmatrix}, \qquad \boldsymbol{c}^{TI} = \begin{bmatrix} \boldsymbol{c}_T & 0 \\ 0 & \boldsymbol{c}_{II} \end{bmatrix}, \qquad \boldsymbol{k}^{TI} = \begin{bmatrix} \boldsymbol{k}_{TT} & \boldsymbol{k}_{TI} \\ \boldsymbol{k}_{IT} & \overline{\boldsymbol{k}}_{II} \end{bmatrix} \tag{19a, b, c}$$

$\boldsymbol{m}^{TI}$ is a lumped mass matrix, where half of the element's mass is assigned to the nodal translations of each node. The lumped mass matrix formulation is used to decouple the transition and interface nodal inertia forces. Damping matrix $\boldsymbol{c}^{TI}$ is formulated based on the mass proportional component of Rayleigh damping, where $\boldsymbol{c}^{TI} = a_1 \boldsymbol{m}^{TI}$. Only the mass proportional component is considered because a stiffness component would result in coupling terms that will create large unrealistic damping forces at the interface node due to any initial velocity at the transition node prescribed by Elasto-Dyn. The stiffness matrix of the beam-column element $\boldsymbol{k}^{TI}$ is identical to the existing formulation in [42]. The vectors $\boldsymbol{F}_{i,j}^{IT}$, $\boldsymbol{F}_{i,j}^{DT}$ and $\boldsymbol{F}_{i,j}^{RT}$ in Equation (18) are the inertia, damping, and restoring force components at the transition node.

Step 4 Input $\boldsymbol{F}_{i,j}^{H}$ and $\boldsymbol{F}_{i,j}^{TH}$ from Hydro-Dyn to the coordinator. Determine the internal force at the transition node and return a negative value to Elasto-Dyn that acts of the base of the tower (see Figure 7):

$$\boldsymbol{F}_{i,j}^{TA} = -\left(\boldsymbol{F}_{i,j}^{IT} + \boldsymbol{F}_{i,j}^{DT} + \boldsymbol{F}_{i,j}^{RT} - \boldsymbol{F}_{i,j}^{TH} - \boldsymbol{F}^{TW}\right) \tag{20}$$

$\boldsymbol{F}_{i,j}^{H}$ is the applied hydrodynamic load acting on the analytical and experimental substructures and $\boldsymbol{F}_{i,j}^{TH}$ is that applied to the transition node, all of which are determined by Hydro-Dyn. $\boldsymbol{F}^{TW}$ is the constant self-weight of the OWT above the transition point that is lumped at the transition node in the vertical direction.

Step 5 If $j < j_{max}$, set $j = j + 1$ and repeat Steps 2 through 5. Otherwise, proceed to Step 6.

Step 6 Determine the force $\boldsymbol{F}_{i,j}^{I}$ applied to the analytical substructure at the interface node and the effective load vector associated with the complete set of DOF of the analytical substructure:

$$\boldsymbol{F}_{i,j}^{I} = \boldsymbol{k}_{IT}\boldsymbol{d}_{i,j}^{T}, \qquad \boldsymbol{F}_{i}^{EFF} = \begin{pmatrix} -\boldsymbol{F}_{i,j}^{I} \\ \boldsymbol{0} \end{pmatrix} + \boldsymbol{F}_{i,j}^{H} \tag{21a,b}$$

The vector $\boldsymbol{F}_{i,j}^{I}$ is the external force acting on the interface node due to the deformations between the transition node computed by Elasto-Dyn and that of the interface node.

Step 7 If $i = 0$, then determine the initial acceleration of the analytical and experimental substructures at the interface node:

$$\boldsymbol{a}_{i=0,j} = \left[\boldsymbol{a}_{i=0,j}^{\boldsymbol{I}}\ \boldsymbol{a}_{i=0,j}^{A}\ \boldsymbol{a}_{i=0,j}^{\boldsymbol{E}}\right]^{T} = \boldsymbol{M}^{-1}\left(\boldsymbol{F}_{i=0,j}^{EFF} + \boldsymbol{F}^{AETW}\right) \tag{22}$$

$$\widehat{\boldsymbol{v}}_{i=0,j} = \left[\widehat{\boldsymbol{v}}_{i=0,j}^{\boldsymbol{I}}\ \widehat{\boldsymbol{v}}_{i=0,j}^{A}\ \widehat{\boldsymbol{v}}_{i=0,j}^{E}\right]^{T} = \Delta t\boldsymbol{\alpha}_{1_O}\boldsymbol{a}_{i=0,j} \tag{23}$$

where $\boldsymbol{F}^{AETW}$ is the constant self-weight load vector of the monopile that is lumped at the vertical DOF of each node in the analytical and experimental substructures and the interface node of the transition substructure.

Otherwise, if $i \neq 0$ then determine the velocity-like vector associated with the substructure's DOF:

$$\widehat{\boldsymbol{v}}_{i} = \begin{cases} \boldsymbol{A}_O\left[\boldsymbol{F}_{i-\alpha_f} - \boldsymbol{F}_{ID_{i-\alpha_f}} - \boldsymbol{R}_{i-\alpha_f} - \widehat{\boldsymbol{F}}_{I_{i-1}}\right], & t_i \leq t_{Tr} \\ \boldsymbol{A}_U\left[\boldsymbol{F}_{i-\alpha_f} - \boldsymbol{F}_{ID_{i-\alpha_f}} - \boldsymbol{R}_{i-\alpha_f} - \widehat{\boldsymbol{F}}_{I_{i-1}}\right], & t_i > t_{Tr} \end{cases} \tag{24a,b}$$

where $\boldsymbol{A}$ is defined by Equation (8a), with $\boldsymbol{A}_O$ based on modal damping and $\boldsymbol{A}_U$ Rayleigh proportional damping in accordance with Equation (14). $\boldsymbol{F}_{i-\alpha_f}$ is the weighted applied load vector defined as:

$$\boldsymbol{F}_{i-\alpha_f} = (1-\alpha_f)\boldsymbol{F}_i^{EFF} + \alpha_f \boldsymbol{F}_{i-1}^{EFF} + \boldsymbol{F}^{AETW} \tag{25}$$

The other vector terms appearing in Equation (24) were defined previously in Equation (5). The analytical substructure restoring forces $\boldsymbol{R}_i^a$ and $\boldsymbol{R}_{i-1}^a$ appearing in $\boldsymbol{R}_{i-\alpha_f}$ are numerically computed. The experimental substructure restoring forces $\boldsymbol{R}_i^e$ and $\boldsymbol{R}_{i-1}^e$ which appear in $\boldsymbol{R}_{i-\alpha_f}$ are measured restoring forces of the pile foundation corresponding to $\boldsymbol{d}_i$ and $\boldsymbol{d}_{i-1}$, respectively. $\widehat{\boldsymbol{F}}_{I_{i-1}}$ is the acceleration-like vector, where:

$$\widehat{\boldsymbol{F}}_{I_{i-1}} = \begin{cases} \boldsymbol{B}_O \widehat{\boldsymbol{v}}_{i-1}, & t_i \le T_{Tr} \\ \boldsymbol{B}_U \widehat{\boldsymbol{v}}_{i-1}, & t_i > T_{Tr} \end{cases} \tag{26a, b}$$

where $\boldsymbol{B}$ is defined by Equation (8b). The acceleration can be optionally calculated from:

$$\boldsymbol{a}_i = \begin{cases} \boldsymbol{D}_O \widehat{\boldsymbol{v}}_{i,j}, & t_i \le T_{Tr} \\ \boldsymbol{D}_U \widehat{\boldsymbol{v}}_{i,j}, & t_i > T_{Tr} \end{cases} \tag{27a, b}$$

where $\boldsymbol{D}$ is defined by Equation (8c). The target displacement $\boldsymbol{d}_i^E$ from Equation (16) is imposed onto the pile foundation over j_{max} number of sub-steps using a ramp generator, where:

$$\boldsymbol{d}_{i,j}^E = \boldsymbol{d}_{i-1}^E + \left(\frac{\boldsymbol{d}_i^E - \boldsymbol{d}_{i-1}^E}{j_{max}}\right) * j, \qquad where \;\; j \in (1, \dots, j_{max}) \tag{28}$$

Step 8 If $i = i_{max}$, the corresponding value associated with the predefined time duration, then terminate the RTHS, else set j = 1 and $i = i + 1$ and return to Step 2.

10. MODEL INTEGRATION PARAMETERS

The model integration parameters required by the MKR-α integration algorithm depend on the properties of the experimental substructure. The frequency dependent equivalent stiffness $k_{eq}\ (\omega)$ and damping coefficient $c_{eq}(\omega)$ are determined by subjecting the pile foundation to a predefined sinusoidal displacement input corresponding to the fundamental frequency of 0.25Hz of the OWT at amplitudes of 5mm and 10mm (expected displacement amplitudes of the pile head during the

RTHS). The behavior of the pile foundation when subjected to these conditions under the cyclic displacement is shown in Figure 9, where a hysteresis occurs in both cases.

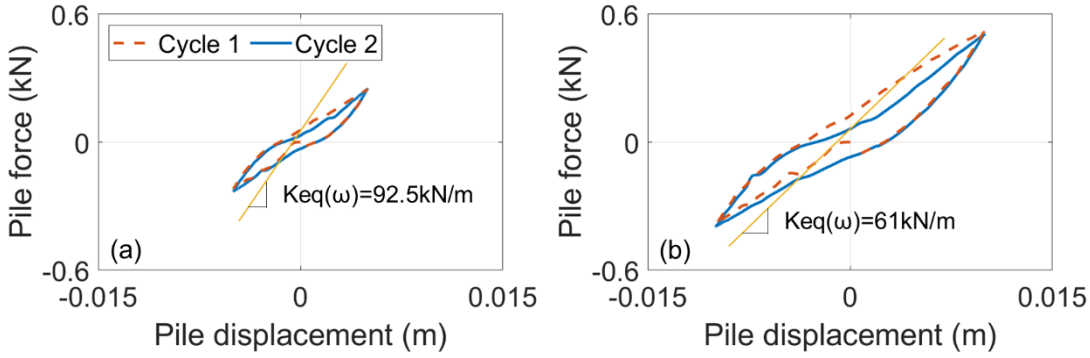

Figure 9: Cyclic behavior of pile foundation at $\omega = 0.25$Hz: (a) 5mm displacement amplitude; and (b) 10mm displacement amplitude.

The equivalent stiffness $k_{eq}(\omega)$ is obtained by examining the maximum force-displacement slope of the pile under the cyclic displacement. This occurred during Cycle 1, as shown Figure 9, where for the 10mm displacement amplitude test the slope of 92.5kN/m is larger among the two tests and assigned to be the value for $k_{eq}\ (\omega)$. $k_{eq}\ (\omega)$ is based on the maximum slope of the force-displacement response in Figures 9(a) and 9(b) because underestimating $k_{eq}(\omega)$ or $c_{eq}(\omega)$ can lead to an instability in the RTHS [64]. The damping coefficient $c_{eq}(\omega)$ is obtained by equating the energy dissipated by the pile foundation in one cycle of motion to that of a single degree of freedom spring-mass oscillator system [40] whereby,

$$c_{eq}(\omega) = \frac{E_D}{\pi\omega u_0^2}, \qquad E_D = \frac{1}{2}\sum_{i=1}^{n}(f_{i+1} + f_i)(u_{i+1} - u_i) \tag{29a, b}$$

In Equation (29a), E_D is the energy dissipation per cycle obtained by numerically integrating the area under the force-displacement curve in Figures 9(a) and 9(b) using the trapezoidal rule (Equation (29b)), ω is the 1st natural frequency of the OWT of $\pi/2$ rad/sec, u_0 is the displacement amplitude of 0.005m and 0.01m, and f_i and u_i are the measured force and displacement, respectively, at the integration time step $i \in (1, n)$. Those two values were used

based on trial RTHS's involving the operational and more severe conditions where the displacement amplitudes during RTHS's reached values approximately equal to the displacement amplitudes of 0.005m and 0.01m. The measured force and displacement were filtered using a 10Hz cut-off frequency low pass filter to remove high frequency noise in the measured signal [57]. The energy dissipation E_D was found to be equal to 6.2x10^{-4}kN-m and 2.4x10^{3}kN-m for $u_0 = 0.005$m and 0.01m, respectively, resulting in a $c_{eq}(\omega)$ value of 5.02kN-sec/m and 4.83kN-sec/m for the two displacement amplitudes. The dimensional scale factor of the pile is 1/120 = 1/ α, and therefore the equivalent stiffness $k_{eq}^{F}\ (\omega)$ and damping $c_{eq}^{F}(\omega)$ coefficients at full scale are equal to:

$$k_{eq}^{F}\ (\omega) = \alpha\mu k_{eq}(\omega), \qquad c_{eq}^{F}\ (\omega) = \alpha^{1.5}\mu c_{eq}(\omega) \tag{30a, b}$$

The quantity μ appearing in Equation (30) is used to investigate the effects of scaling the equivalent stiffness and damping coefficients on the stability of a RTHS, as will be discussed later when presenting the test matrix.

11. VISCOUS DRAG CONTRIBUTION TO EQUIVALENT DAMPING

As previously discussed, the drag force in Morison's equation is proportional to the square of the relative velocity between the structure and fluid particle (see Equation (2)). Hence, the fluid drag forces that are imposed on the analytical substructure need to be accounted for when calculating the model integration parameters to ensure a stable RTHS. Considering the drag force in Equation (2), the drag force F_d associated with a tributary member nodal length L is shown in Equation (31a).

$$F_d = \frac{1}{2}\rho C_d A(v_f - v_s)\left|v_f - v_s\right|, \qquad F_{dL} = \frac{1}{2}\rho C_d A\sqrt{\frac{8}{\pi}}\ \sigma_{v_r}\ (v_f - v_s), \qquad \sigma_{v_r} = \frac{1}{\sqrt{2}}v_{r_0} \tag{31a, b, c}$$

In Equation (31a), A is the tributary area equal to DL where L is the nodal tributary length, D is the diameter of the monopile, and as noted above v_f is the fluid particle velocity and v_s the

structural velocity. Linearizing this nonlinear drag term [65, 66] leads to F_{dL} that is given by Equation (31b), where σ_{v_r} is the standard deviation of the relative velocity v_r between the water particles and the structure. For a steady state condition, v_r is periodic with a zero mean and $\sigma_{v_r} = \frac{1}{\sqrt{2}} v_{r_0}$ (see Equation (31c)), where v_{r_0} is the amplitude of the steady state relative velocity. Hence,

$$F_{dL} = \frac{1}{2}\rho C_d A \sqrt{\frac{4}{\pi}}\, v_{r_0} v_f - \frac{1}{2}\rho C_d A \sqrt{\frac{4}{\pi}} v_{r_0} v_s\,, \qquad c^v = \frac{1}{2}\rho C_d A \sqrt{\frac{4}{\pi}} v_{r_0} \tag{32a, b}$$

The second term in Equation (32a) is proportional to the structural velocity, and thus when moved to the left-hand side of the equations of motion is associated with the hydrodynamic damping coefficient c^v defined in Equation (32b). The elements of the viscous drag matrix $\boldsymbol{C}^v$ are based on Equation (32b) to calculate the model integration parameters. In accordance with Kolay [9] and Kolay et al. [62], it is imperative that conservative assumptions therefore be used in estimating c^v, since it will affect the value of the integration parameters. If c^v is underestimated than an instability in the RTHS can occur. A conservative value for the damping coefficient $\boldsymbol{C}^v$ is obtained by assuming the fluid particle and structural velocities are 180 degrees out of phase, whereby the maximum value for the relative velocity is $(v_{r_0})_{max} = \left|v_f\right|_{max} + |v_s|_{max}$ and $|*|_{max}$ denotes an absolute maximum value. Based on the characteristics of deep water and intermediate waves, $\left|v_f\right|_{max} = h\omega$ [50], where h and ω are the wave amplitude (half the wave height) and frequency, respectively. The wave period used in the RTHS is 10sec., leading to peak fluid particle velocities at the mean water surface of $\left|v_f\right|_{max} = 3.77$m/sec and 7.54m/sec for the two wave heights of 6m and 12m, respectively, which are the two wave heights used in the RTHS test matrix presented in Section 13. The peak structural velocity $|v_s|_{max}$ is calculated based on the elastic structural deformations of the monopile combined with the maximum allowable pile rotation at the mudline of 0.5 deg under hydrodynamic loading [67]. This amount of pile rotation results in a

0.175 m rigid body motion at the water surface for the full-scale structure. The elastic deformations of the monopile due to the applied hydrodynamic forces were conservatively estimated by assuming that the monopile from the mudline to the water surface is subjected to a linear varying lateral distributed load causing a stress of 100% of the monopile's yield strength at the mudline (the monopile is designed to remain elastic under the loading conditions used in the RTHS). The resulting displacement from the elastic deformations is 0.039 m at the water surface for the full-scale structure, and considerably smaller than the displacement from rigid body motion. Assuming the monopile to be vibrating in its fundamental mode at the frequency of $\pi/2$ rad/sec, the $|v_s|_{max}$ at the water surface was found to be of 0.33 m/sec for the full-scale structure. To estimate $(v_{r_0})_{max}$ over the submerged length of the monopile, the $|v_s|_{max}$ was calculated along the monopile and $|v_f|_{max}$ was calculated assuming the fluid particle velocity to decrease linearly with water depth. This results in larger values for $|v_f|_{max}$ with increasing water depth compared to where the fluid particle velocity decreases exponentially as assumed in linear wave theory. Consequently, a more conservative estimate of $\boldsymbol{C}^v$ is obtained compared to where the actual fluid particle velocity decreases at the faster exponential rate.

12. SYNCHRONIZATION AND DATA TRANSFER BETWEEN OPENFAST AND SIMULATION COORDINATOR

The simulation coordinator was created using Simulink [57] and compiled and then run in real-time on the simulation computer. OpenFAST and the Simulink model resided on the same Dell computer that was equipped with an Intel i-9 processor and 32 gigabytes of random-access memory. The synchronization of data transfer between OpenFAST and Simulink is achieved using the *Windows Application Programming Interface* (API) functions with file mapping objects [68]. The process is shown schematically in Figure 10 and explained below. The data is written-to and

read-from memory mapped objects in order to synchronize the data exchange between the simulation coordinator and OpenFAST in real-time. The Simulink feature *Set Pace* is used to pace the simulation to match that of a real-time simulation. The *C-Caller* block in Simulink (written in C programming language) is used to write-to and read-from the memory mapped files shared with OpenFAST. Intel's FORTRAN compiler ability to bind code written in C programming language is used to enable OpenFAST, which is written in the FORTRAN programming language, to read and write to the memory mapped objects [69]. As mentioned previously, a SCRAMNet memory card is integrated with the computer system to allow fast communication between Simulink and the xPC target machine which controls the command displacement to the electric actuator.

Synchronization of the data transfer is achieved using the Windows API functions *CreateEvent*, *SetEvent*, *WaitForSingleObject*, and *ResetEvent.* OpenFAST first creates the file mapping object using the API function *CreateFileMapping* and writes the data to the mapped object using the *MapViewOfFile* API function. It then signals the readiness of the data to Simulink using the *SetEvent* function. Simulink waits for the data to be written to the memory mapped object through the API function *WaitForSingleObject*. Once Simulink receives the signal that the data is ready to read, the *C-Caller* block in Simulink opens the file mapping object using the *OpenFileMapping* API function and reads the content of the memory mapped object shared with OpenFAST using the *MapViewOfFile* API function. Once Simulink reads the data it triggers the event using the *SetEvent* API function to inform OpenFAST that the data has been successfully read. This process is reversed, where after Simulink completes the required computations it writes the data to a memory mapped object which is then subsequently read by OpenFAST.

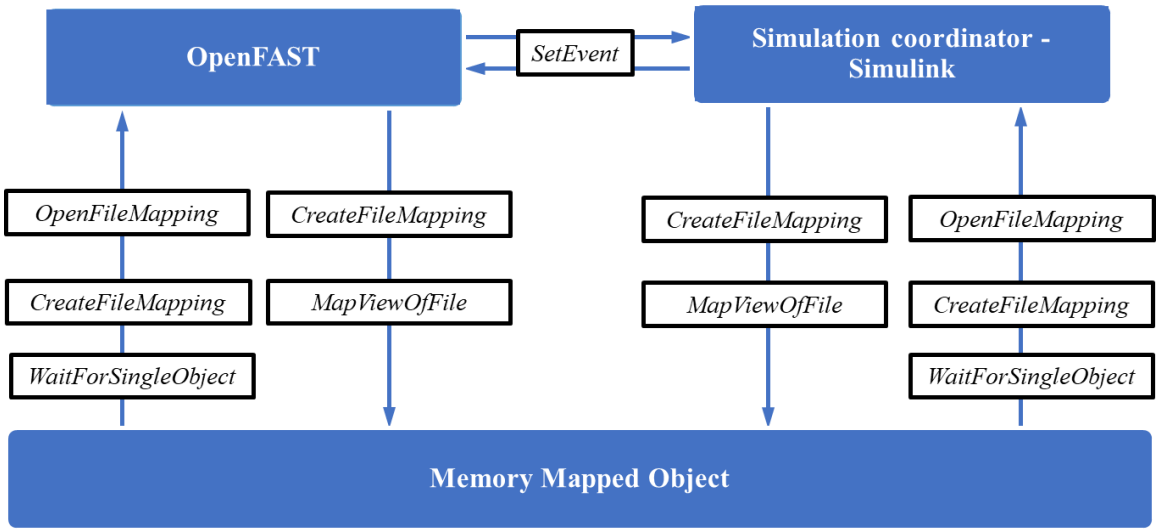

Figure 10: Data exchange between the simulation coordinator and OpenFAST using memory mapped objects.

The time step size of Δt =3/1024 sec. used in the RTHS herein does not guarantee a strict real-time performance during all RTHS because of the indeterministic nature of OpenFAST calculations. The simulation coordinator is designed to track the wall clock time needed by OpenFAST to complete each integration step. In all RTHS results reported in this paper, OpenFAST managed to complete the integration process faster than real-time, and therefore the simulation coordinator was able to slow the simulation to match real-time performance. Because of the multiple user options in OpenFAST, it is not possible to conclude that OpenFAST can achieve a real-time performance under all scenarios. Exploring such a topic is outside the scope of the current work and treatment of this issue may require either running OpenFAST on a high-end computer, increasing the integration time step, simplifying the model in OpenFAST to reduce the computational cost, and/or making use of OpenFAST's ability to perform parallel computations.

13. RTHS TEST MATRIX

The RTHS test matrix is given in Table 1. It includes several tests in order to assess the RTHS when subjecting the OWT to several different load scenarios of operational and more severe conditions. The operational conditions of the OWT are included in Tests 1, 2, and 3 involve a

steady wind speed and regular wave height of 12m/s and 6m, respectively, while the more severe conditions are associated with Test 4 and involve a wind speed of 20m/s and a regular wave height of 12m. The hydrodynamic and aerodynamic loading were imposed in the same direction, which was perpendicular to the plane that the OWT blades rotate in. The test matrix was developed to also assess the recommended approach presented in Section 10 to estimate the equivalent stiffness $k_{eq}\ (\omega)$ and damping coefficient $c_{eq}\ (\omega)$ of the pile foundation. As noted previously, the RTHS framework uses an explicit model-based integration algorithm where $k_{eq}^{F}\ (\omega)$ and $c_{eq}^{F}\ (\omega)$ of the experimental substructure are required to determine these model integration parameters. Underestimating these can lead to an instability of the RTHS [64]. The testing matrix is intended to evaluate the sensitivity of the recommended approach for estimating $k_{eq}^{F}\ (\omega)$ and $c_{eq}^{F}\ (\omega)$ by using the factor μ in Equation (30) to scale up and scale down $k_{eq}(\omega)$ and $c_{eq}(\omega)$ by a factor of 2.0 and 0.5 in Tests 2 and 3, respectively (see Table 1). Each test has a duration of 600 seconds and was performed in the sequence listed in Table 1.

Table 1: RTHS test matrix.

Test ID	Wind speed (m/s)	Wave height (m)	$k_{eq}(\omega)$ (kN/m)	$c_{eq}(\omega)$ (kN-sec/m)	μ
1	12	6	92.5	5.02	1.0
2	12	6	92.5	5.02	2.0
3	12	6	92.5	5.02	0.5
4	20	12	92.5	4.83	1.0

14. RTHS COORDINATOR ASSESSMENT

The validation of the RTHS coordinator includes comparing the OWT response from an independent OpenFAST analysis (i.e., a reference solution) with the response from the RTHS platform used in this paper. The OpenFAST module Sub-Dyn cannot be used to analyze an OWT monopile and foundation with nonlinear mechanical behavior [42]. In this comparison the OWT had a linear foundation modeled using linear elastic springs. For the reference solution the OWT

was entirely modeled and analyzed using the OpenFAST to acquire the response identified as *Reference*. For the RTHS, the simulation involved an *electric-off mode* and referred to as *RTHS-EO*, where instead of sending the target displacement to the pile in the soil box and measuring the corresponding restoring force, the restoring force of the pile is obtained by multiplying the target actuator displacement command from the RTHS coordinator by the same stiffness of a linear pile used in the Reference solution. In addition, the modal damping during the first 120 seconds was omitted in the *RHTS-EO*. This will create two comparable analytical models where the results from the RTHS-EO can be compared to those from the OpenFAST Reference structure. The pile has a linear spring with a stiffness of k_x= 11.1E+3kN/m in the direction where the experimental substructure is oriented. The stiffness k_x is obtained from Equation (30a), where $\alpha = 120$, $\mu = 1$, and $k_{eq}(\omega)$ is 92.5 kN/m. The compliance of the foundation for the remaining degree of freedoms is accounted for in the same manner as that used for the RTHS, which was explained earlier in Section 9.

Figure 11 shows the time history of the hub displacement obtained from the Reference solution and that from the RTHS-EO plotted at full-scale. The normalized root mean square error (NRMSE) [6, 9, 64] between the two results is 0.23% and 0.30% in the along-wind and the cross-wind directions, respectively. This error is small and it is evident that the RTHS platform accurately captures the dynamics of the OWT. Sources of possible error that can lead to an inaccurate RTHS would include actuator control, state determination nonconvergence, and communication delay between the workstations in the integrated control architecture [7, 8]. None of these errors occurred in the RTHS-EO, and will be discussed more in the section that presents the RTHS results. The minute difference between the results is attributed to OpenFAST accounting for dynamics of the monopile below the transition piece using the Craig-Bampton method [41],

which is a truncated modal solution. The RTHS formulation integrates the equations of motion considering the full set of degrees of freedom of the system and therefore captures a more complete solution.

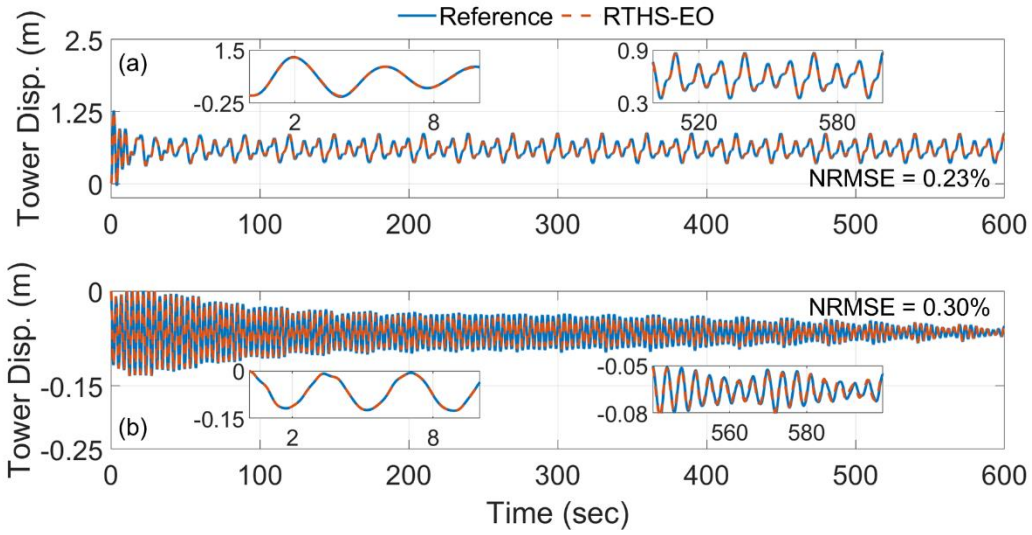

Figure 11: Displacement time history of the top of the tower (at the hub in Figure 2) in the (a) along-wind, and (b) cross-wind directions for a OpenFAST linear reference structure and the RTHS of the same structure.

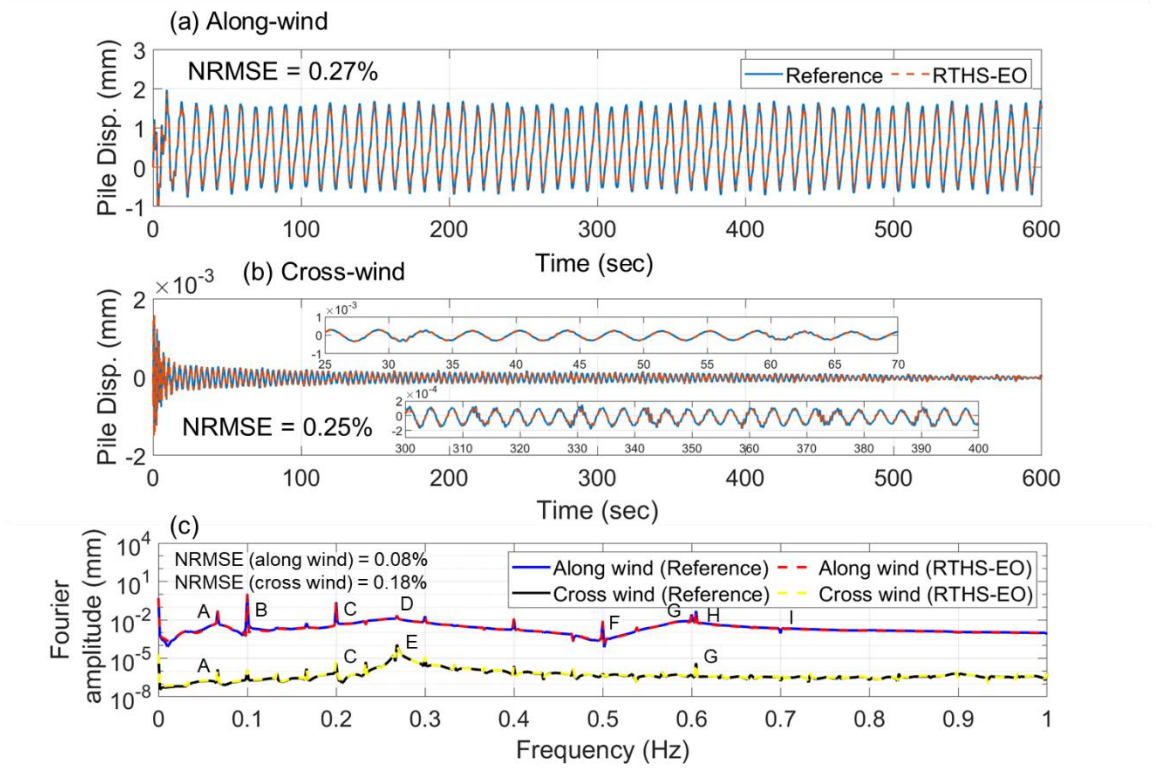

Figure 12: Comparison of Reference solution and RTHS-EO results for pile head displacement time histories in (a) along-wind and (b) cross-wind direction, and (c) frequency decomposition of pile head displacement (semilog-scaled).

Table 2: Natural structural frequencies, steady state aerodynamic and mechanical equipment vibration loading frequencies.

Label	Frequency (Hz)	Description
A	0.067	Energy equipment vibration – rotor speed controller
B	0.10	Wave frequency
C	0.20	1P aerodynamic load
D	0.247[(a)]	1st mode support structure fore-aft
E	0.267	1st mode support structure side-to-side
F	0.50	Energy equipment vibration – blade pitch angle controller
G	0.60	3P aerodynamic load
H	0.620	1st mode blade asymmetric flapwise pitch
I	0.697	1st mode blade collective flap

(a) Equal to 0.202Hz for RTHS

The pile head displacement time histories in the along-wind and cross wind directions are shown plotted at the experimental substructure's scale in Figures 12(a) and (b), respectively, for the Reference solution and RTHS-EO results. Similar to Figure 11, exceptional agreement between the comparison of the Reference solution with the RTHS-EO results is seen in Figure 12(a) and (b), where the NRMSE error is 0.27% and 0.25% in the along-wind and cross-wind directions, respectively. The along-wind pile head displacement appears to be dominated by the 0.1Hz steady-state hydrodynamic loading. The frequency decomposition of the pile head displacement is shown in Figure 12(c). The NRMSE between the Reference solution and RTHS-EO results for the frequency decomposition for the along-wind and cross-wind is 0.08% and 0.18%, respectively, and are considered to be small. The frequency decomposition includes the effects of energy at the wave loading frequency, aerodynamic loading frequencies, frequencies of vibration from the energy generation equipment, and modal frequencies of the OWT. The frequencies associated with these phenomena are summarized and labeled in Table 2 up to 1Hz. The natural frequencies of the OWT were determined from modal testing using a RTHS-EO approach where a band-limited white noise load with a frequency range of 0 to 35Hz was applied to the monopile, and the Fourier analysis of the recorded displacements was performed. The Fourier amplitude shown in Figure

12(c) covers the frequency range from 0 to 1Hz, which is the range of the natural frequencies within what the OWT that were observed to participate in the RTHS. Data was recorded at each time step of Δt = 3/1024sec. (i.e., 1024/3Hz) over a 600sec. duration. The pile head displacement had an RMS value of 0.88mm. The frequency decomposition was calculated using 204800 Fast Fourier Transform (FFT) points, resulting in a frequency resolution of (1024/3)/204800 ≈ 0.002Hz. Four natural frequencies were found over the frequency range of 0 to 1Hz and are included in Table 2 (where they are labeled with letters): 1st mode support structure fore-aft at 0.247Hz (D); 1st mode support structure side-to-side of 0.267Hz (E); 1st mode blade asymmetric flapwise pitch at 0.620Hz (H); and the 1st mode blade collective flap at 0.697Hz (I). The higher modes outside this frequency range are not presented herein since the participation of these modes was minimal, and is discussed below. Details of the natural mode shapes and higher modes can be found in Shi et al. [70].

The Fourier amplitude at 0.067Hz (A) shown in Figure 12(c) is associated with energy generation equipment mechanical vibrations created by the rotor speed controller. The dominance of the wave energy is evident in the frequency decomposition of the pile head displacements, where the peak energy in the plot occurs in the along-wind direction at 0.1Hz (B). A resonance is present near 0.247Hz (D) in the along-wind direction associated with the OWT 1st fore-aft mode. In the cross-wind direction a rise in energy also occurs near the frequency of 0.267Hz (E) and is associated with response resonance in the vicinity of the fundamental frequency of the OWT side-to-side 1st mode. The spikes in the Fourier amplitude at 0.2Hz (C) and 0.6Hz (G) are associated with the 1P and 3P aerodynamic loading frequencies, respectively, caused by the 12 rpm rotor speed, where the 1P is related to one complete revolution of the set of blades and the latter the frequency of one of the blades passing the tower which creates a shadowing effect and alters the

aerodynamic loading on a blade [71]. Labels H and I are associated with the 1st mode blade asymmetric flapwise pitch at 0.620Hz and the 1st mode blade collective flap at 0.697Hz, respectively. Small spikes in energy appear periodically throughout the frequency decomposition at a spacing of 1/30Hz and are associated with vibrations caused by a mechanical controller adjusting the blade's pitch angle to sustain the 12rpm rotor speed. The energy spikes associated with these vibrations are observed to be most noticeable at a frequency spacing of 0.1Hz over the frequency range of 0.1 to 0.5Hz, with the spike at 0.5Hz (F) the most prominent.

The modes of the OWT that appear in the Reference solution and RTHS-EO to have the most noticeable dynamic amplification that contribute to the pile along-wind displacement are those with the lowest frequencies, and include the support structure fore-aft 1st mode (D) and the blade asymmetric flapwise pitch 1st mode (H). In the cross-wind direction a noticeable dynamic amplification is seen in the support structure side-to-side 1st mode (E). The remaining 1st mode blade collective flap (I) appears to have minimal dynamic amplification in the Reference solution and RTHS-EO results.

15. HYBRID SIMULATION RESULTS

The along-wind measured pile head displacement and force time histories of all of the RTHS tests are shown plotted at the experimental structure's scale in Figures 13 and 14, respectively. The displacements are the scaled displacements imposed to the experimental substructure and the force is the measured force in the actuator load cell prior to being scaled up to full scale. In Tests 1 through 4 the amplitude of the pile displacement is small at the start of the RTHS because of the effect of the supplemental modal damping during the first 120 seconds of each test. The pile displacement time histories are shown to be nearly identical for Tests 1, 2, and 3. The small discrepancy between the tests is attributed to the difference in the soil condition of each subsequent

tests. A shift and drift in the pile displacement and force from their initial zero values for Tests 1, 2, and 3 is seen in Figures 13 and 14, and occurs in the direction of the hydrodynamic and aerodynamic loading. A comparison with the Reference solution for the pile head displacement is shown in Figure 13, where the Reference solution model is subjected to the same hydrodynamic and aerodynamic loads as the respective RTHS. The Reference solution displacements in Figure 13 are shown to be smaller in amplitude than those of the RTHS and illustrate the importance of accounting for nonlinear behavior in the foundation.

The results of Tests 1, 2, and 3 indicate that the range of the values used for the model integration parameters in Table 1 are within the permissible range to ensure stability of the MKR-α integration algorithm applied to the OWT RTHS. Test 3 did not go unstable even though the model integration parameters are intentionally underestimated. This is due to the fact that the stability limit of the MKR-α integration algorithm also depends on damping and mass when $\rho_\infty <$ 1 [9, 64], and the added hydrodynamic mass and damping improve the stability limit. As Kolay showed [64], considering a single degree of freedom system for simplicity, stability is assured when $k_t \leq 2k + \frac{4m}{\Delta t^2}$ for $\rho_\infty = 1$, and when $k_t \leq \left(\frac{4}{3}\right)\left(k + \frac{c}{\Delta t} + \frac{3m}{\Delta t^2}\right)$ for $\rho_\infty = 0$, where k_t is the actual stiffness of the system encountered during a RTHS. The terms on the right-hand side of these inequalities are the model properties that the integration parameters are based on. The mass *m* is divided by the square of the time step size Δt, and thus is the more dominant term on the right-hand side of the inequality that establishes the stability limit. Considering the topography of the mass, stiffness, and damping matrices and their relationship to the DOFs, the analytical substructure model mass, stiffness, and damping terms are larger than those at the DOF shared with the pile foundation (i.e., $k_{eq}^F\ (\omega)$, and $c_{eq}^F\ (\omega)$). Hence, the added hydrodynamic mass dominates the stability limit for the RTHS of the OWT structural system.

The time histories of the pile head displacement and force for Test 4, shown in Figure 13(b) and (d), and Figure 14(b) and (d), respectively, is larger in magnitude than that for the other tests due to the more greater wind speeds and wave height. There is an occurrence of some shifting in the pile displacement and force from their initial zero values for Test 4 that was also present in the other tests. In addition, there is a slight deterioration in the amplitude of the pile force associated with the direction of the hydrodynamic and aerodynamic loading. This phenomenon is associated with the residual deformations and mobilization of localized shear failure in the soil surrounding the pile. The comparison with the Reference solution for the pile head displacement shown in Figure 13(b) and (d) indicates that the difference between the RTHS results and the Reference solution is greater in Test 4 compared to the other RTHS, which further illustrates the importance of accounting for nonlinear behavior in the foundation of an OWT.

The pile head force-displacement response during the RTHS is shown plotted at the experimental structure's scale in Figure 15. The cyclic response is seen to be nonlinear, where in all of the RTHS there is a presence of accumulated pile displacement with a shift towards the positive displacement in the direction of the loading, along with pinching in the hysteresis loops. The degree of shifting and pinching is more predominant in Test 4, which had the more severe conditions for wind speed and wave height causing larger deformations and nonlinear behavior to develop in the pile foundation.

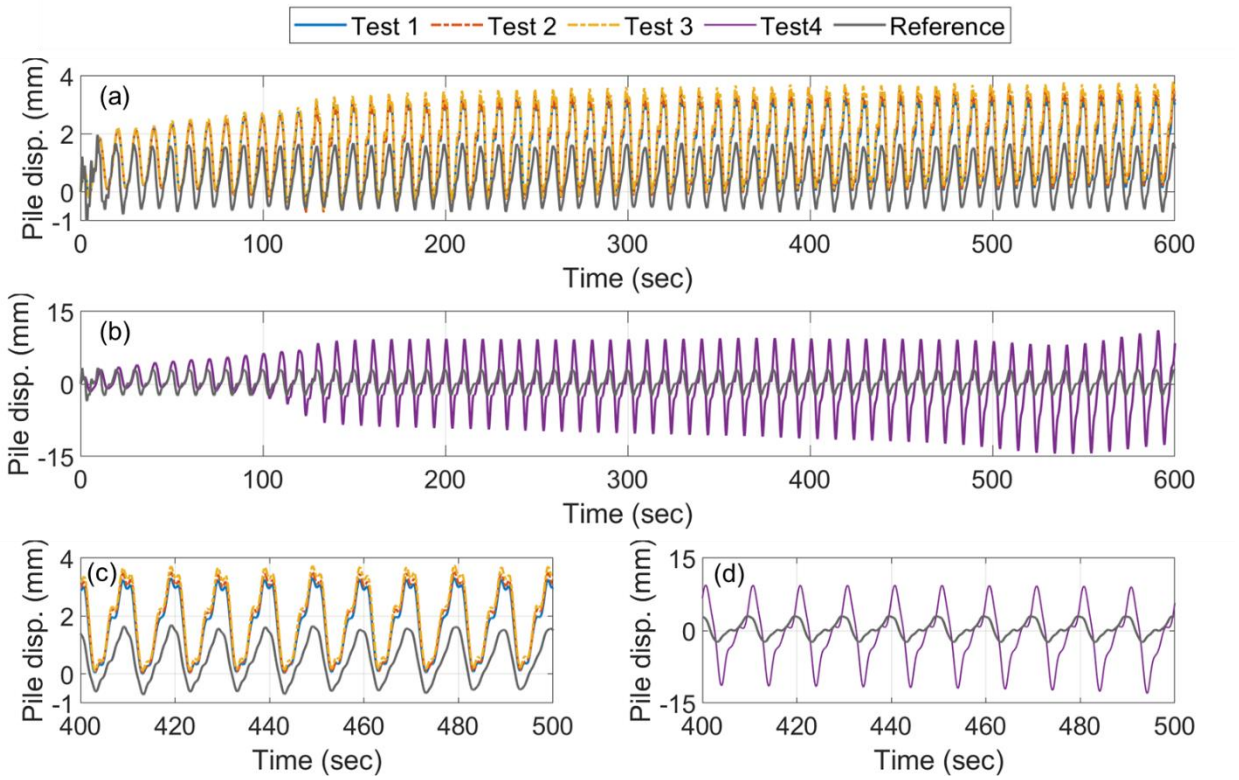

Figure 13: Along-wind pile head displacement history: (a) Tests 1 through 3; (b) Test 4; and, zoomed in view for duration 400 to 500 seconds for (c) Tests 1 through 3, and (d) Test 4.

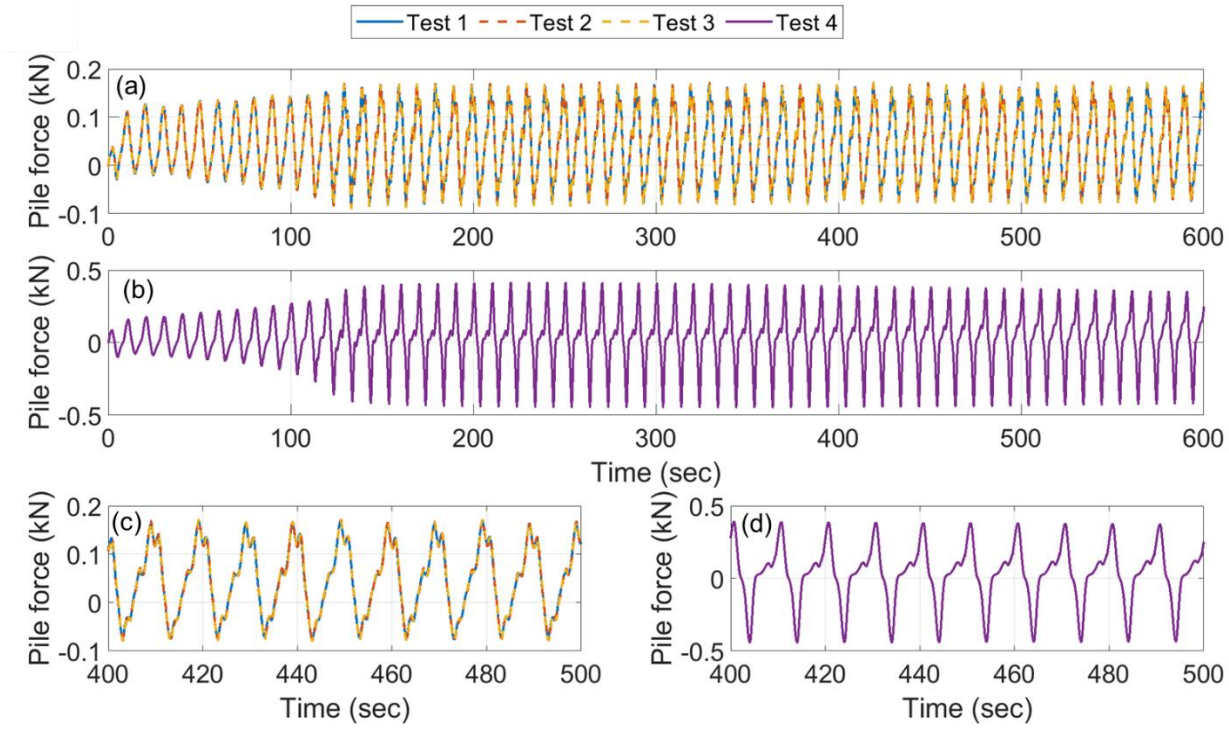

Figure 14: Along-wind pile force history: (a) Tests 1 through 3; (b) Test 4; and, zoomed in view for duration 400 to 500 seconds for (c) Tests 1 through 3, and (d) Test 4.

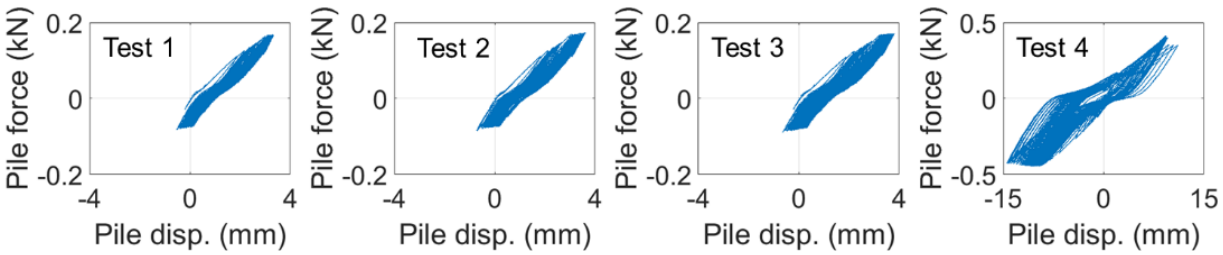

Figure 15: Pile head force-displacement response for Tests 1 through 4.

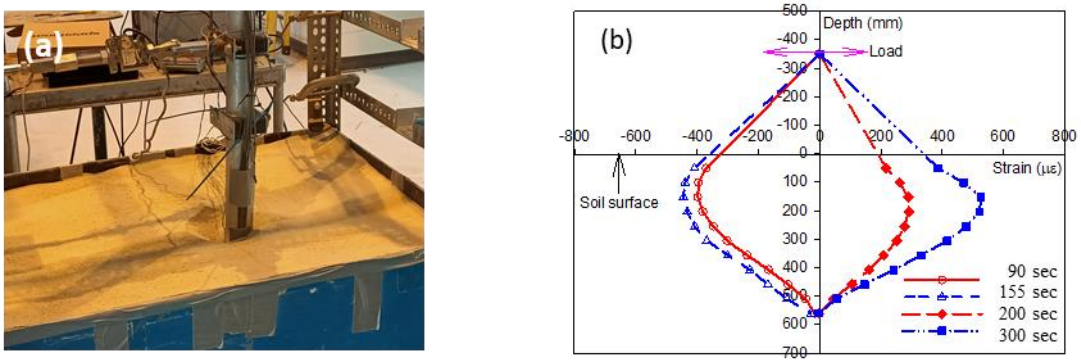

Figure 16: (a) Photograph taken of pile-foundation during Test 1 showing surface soil movement around the pile, and (b) measured strains along pile at selected times during the RTHS.

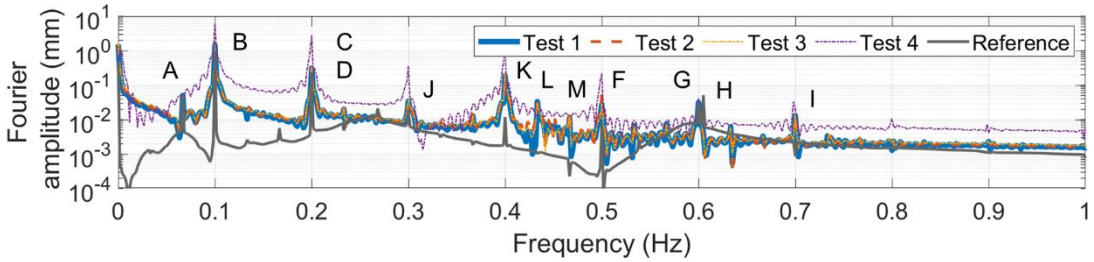

Figure 17: Frequency decomposition of the along-wind pile head displacement (semilog-scaled).

A photograph taken during Test 1 is shown in Figure 16(a). The pile-foundation can be seen leaning towards the right in the photograph (in the direction of the hydrodynamic and aerodynamic loading). The near-surface soil failure around the pile is evident and caused by the cyclic loading of the pile-foundation under the hydrodynamic and aerodynamic loading during the RTHS. The distribution of longitudinal strains over the pile depth is given in Figure 16(b). These strains were measured on the surface of the pile using strain gages. The strain distribution at each time frame is seen to increase beneath the soil surface with depth, reach a maximum strain at approximately three pile diameters below the soil surface, and then decrease to zero at the tip of the pile. It is

worth noting that the measured strains were smaller than the yield strain of the aluminum pile and the pile remained elastic during all of the RTHS.

The frequency decomposition of the pile head along-wind displacement during the RTHS and that for the Reference solution is shown in Figure 17. Only the along-wind displacements of the pile head are included in Figure 17, since they are associated with the measured displacements from the RTHS. As in Figure 12 shown previously, the frequency decomposition in Figure 17 includes the effects of energy at the wave loading frequency, aerodynamic loading frequencies, frequencies of vibrations caused by the operation of the energy generation equipment, and modal frequencies of the OWT. The frequency labels were defined previously in Table 2. The natural frequencies of the OWT for the RTHS were obtained from modal testing of the OWT using a RTHS approach with a 35Hz band-limited white noise load applied to the structure, similar to that described previously for the Reference solution results presented in Figure 12, except that for the RTHS the pile-foundation was modeled physically using the experimental substructure. There are a number of similar trends in the RTHS results compared to the Reference solution that were previously discussed. The peak Fourier amplitude in the RTHS is again at 0.1Hz (B), which is associated with the OWT steady state response to the hydrodynamic loading imposed in the along-wind direction. Spikes in energy occur associated with the 1P and 3P aerodynamic loads (C and G) and energy generation mechanical equipment vibration loads (A). There is a greater amount of energy in the RTHS due to the larger OWT displacements (see Figures 13 and 18) and velocities that develop in the RTHS compared to the Reference solution. The frequency decomposition result in Figure 17 shows the lower modes with natural frequencies up to 0.697Hz to have the most noticeable dynamic amplification and contribution to the along-wind pile displacement. These modes include the support fore-aft 1st mode at 0.202Hz (D), the blade asymmetric flapwise pitch

1st mode at 0.620Hz (H), and the blade collective flap 1st mode at 0.697Hz (I). The natural frequency of the fore-aft 1st mode shifted to 0.202Hz in the RTHS due to the effect from the nonlinear soil behavior which reduced the soil stiffness. For RTHS Test 4, which involved more extreme wave and wind loading, an increase in the energy in the frequency decomposition occurs compared to the other RTHS Tests 1, 2, and 3. A larger Fourier amplitude in the displacement response occurs at 0Hz in the RTHS compared to the Reference solution. This is due to the accumulation of pile displacements and drifting of the pile as damage to the soil occurs during the RTHS. This can be seen in the pile head force-displacement response of the RTHS, Figure 15. The increase in the OWT motion in the RTHS led to greater a mounts of contributions of energy at 0.1Hz, 0.2Hz, 0.3Hz, 0.4Hz, 0.43Hz, 0.46Hz, and 0.5Hz that are labeled B, C, J, K, L, M, and F in Figure 17, respectively, compared to the Reference solution. This phenomenon is associated with the blade angle pitch control, and as explained previously, caused by the blade pitch angle controller introducing mechanical vibrations in an attempt to maintain the 12 rpm rotor speed. The significant differences between the Reference solution and RTHS results illustrates the importance of accounting for nonlinear behavior in the pile foundation of an OWT.

The displacement time histories of the top of the tower (at the hub in Figure 2) in the along- and cross-wind directions are shown plotted at full-scale in Figure 18. Note that the cross-wind direction tower displacements (Figures 18(b) and (d)) are much smaller than the along-wind tower displacements (Figures 18(a) and (c)). The displacement amplitude seen in Figures 18(c) and (d) is higher for Test 4 compared to the first three tests because of the higher wind speed and wave height in the latter test. Modal damping is seen to have an effect on the tower movement in the along-wind direction during the first 120 seconds, and is more noticeable in Test 4 (Figure 18(c)). The cross-wind direction displacement response included an offset in the displacement due to the

wake steering (i.e., the blades of the OWT are facing the wind at a slight angle), Figures 18(b) and (d). Like the pile head displacement time history results for Test 3, the along-wind direction tower displacement time history in Test 4 is dominated by the increased cyclic hydrodynamic loading. The along-wind direction results for all of the RTHS show a steady state response at 0.1Hz associated with the wave period of 10secs. The RTHS results are compared in Figure 18 to the Reference solution for the same wind and wave conditions as that in each of the RTHS. Note that the Reference solution has some transient response at the beginnng of the analysis before achieving steady state because it does not incorporate modal damping over the first 120sec. duration at the start of the analysis. This leads to the cross-wind displacements for the Reference solution to be momentary greater than the RTHS Test 4 results which had the additional modal damping for the first 120sec. of the simulation. The difference between the Reference solution and RTHS results is evident in both the along wind direction (Figures 18(a) and (c)) and the orthgonal cross-wind direction (Figures 18(b) and (d)). The difference between the RTHS and Reference solution results is larger for Test 4 that the other RTHS due to the more severe hydrodynamic and aerodynamic loading conditions for Test 4 that leads to more extensive nonlinear movment of the pile head. Note that the Reference solution for Test 4 involved the same hydrodynamic and aeroelastic loading as the RTHS. These results illustrate the importance of accounting for nonlinear response in the pile foundation of a OWT.

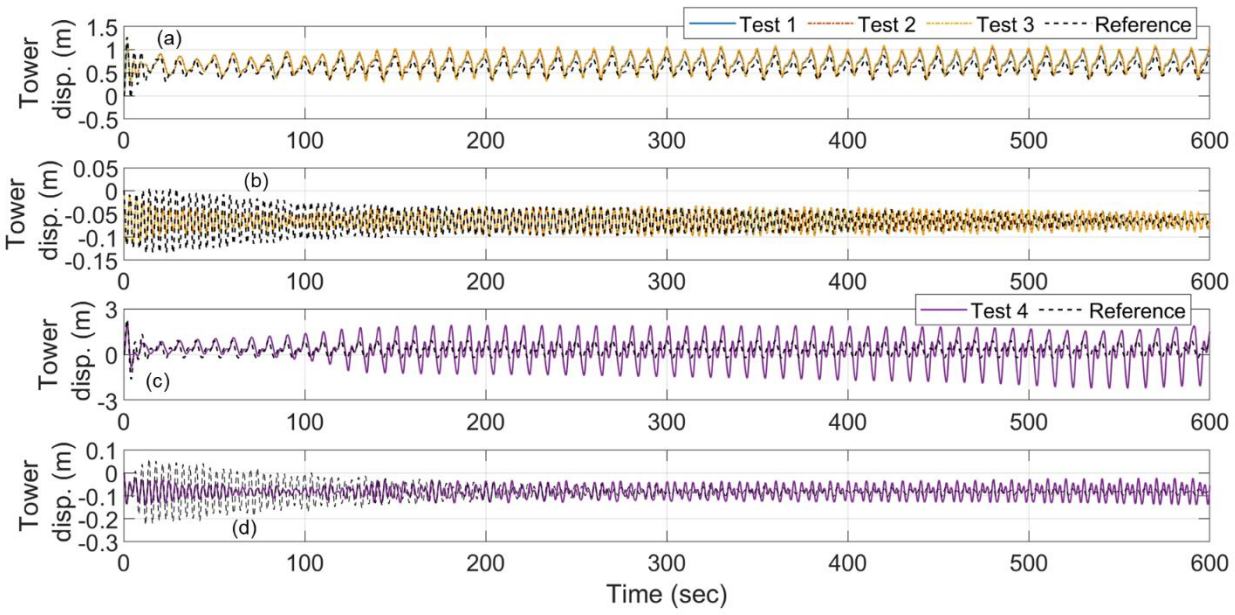

Figure 18: Displacement time history of the top of the tower (at the hub in Figure 2) in the along-wind (a, c), and cross-wind directions (b, d).

16. ASSESSMENT OF RTHS RESULTS

Figure 19 shows synchronized subplots of the target displacements plotted against the measured displacements of the pile for all RTHS. Figure 19 incorporates the entire delay in the RTHS system, which includes any actuator, restoring force, and communication delays. All of the plots show a line that is inclined at 45 degrees, suggesting excellent actuator control was achieved for each RTHS and indications that there was minimal delay and amplitude error in the actuator in the simulations. Actuator amplitude error and delay effects the accuracy of the results of a RTHS, where negative damping that leads to can lead to an instability of the RTHS. The NRMSE, labeled as *J* in the plots, is shown to be small and range from 0.12% to 0.17%.

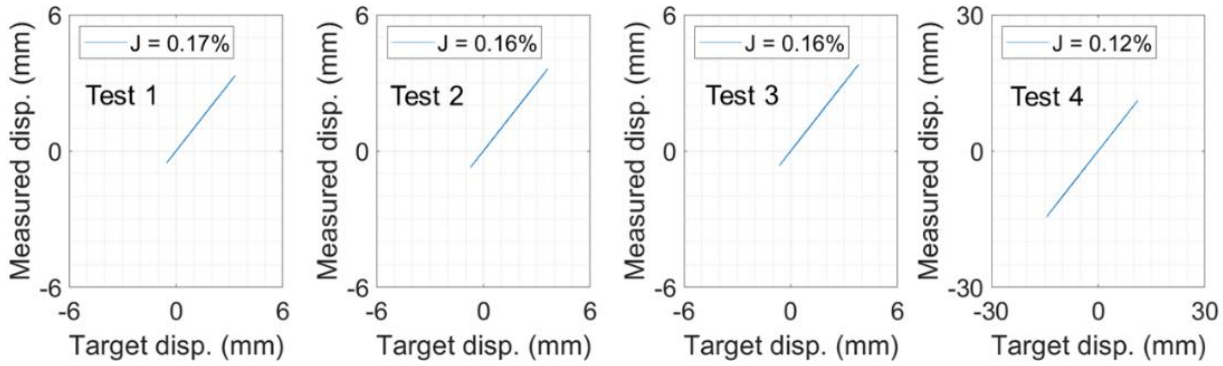

Figure 19: Synchronized target and measured displacements of the pile head during hybrid simulations.

The maximum actuator amplitude error and average time delay observed in the RTHS was less than 1% and about 5msec., respectively, which was determined by comparing the time histories of the target command and measured actuator displacements. To further assess actuator delay, the time delay in the form of a phase plot converted to time delay in the frequency domain was investigated, and presented previously in Figure 6. As noted previously, the time delay had an average value of 5.4msec. between the frequency range of 0 to 3Hz. The average delay observed in the time delay plotted in the frequency domain in Figure 6 is consistent with that observed in the RTHS. As also noted previously the frequency response function of the system had essentially a magnitude of one over the frequency range of 0 to 3Hz, implying that there was no amplitude error in the actuator displacement. A majority of the average time delay of 5.4msec. is attributed to the 2/400sec. communication delay in the RTHS Integrated Control Architecture discussed previously.

To assess the impact that actuator delay has on the quality of RTHS results, a parametric study was performed using the electric-off simulation mode (i.e., RTHS-EO). The study involved systematically introducing a constant delay in the experimental substructure's restoring force feedback signal to the integration algorithm and performing a RTHS-EO based on Test 1 wind speed and wave height conditions. The selected amount of delay was based on multiples of the

time step Δt of 3/1024sec. ranging from 0 to 18/1024sec., and included 0, 3/1024, 6/1024, 9/1024, and 18/1024sec. The time history results for the pile head displacements in the long wind direction are shown plotted in Figure 20. The NRMSE for each simulation are summarized in Table 3, where the RTHS-EO with no delay is considered as the reference solution for the NRMSE calculation. The results show that a time delay of 3/1024sec. (i.e., 2.93msec.) has a small NRMSE value of 0.058%. The NRMSE is shown to increase in Figure 20 and Table 3 as the time delay is increased, where at a 6/1024, 9/1024, and 18/1024sec. delay the NRMSE is 0.120%, 0.185%, and 0.408%, respectively. An NRMSE of 0.12% for the delay of 6/1024sec. is considered small, and therefore the smaller average time delay of 5.4msec. observed in the system FRF has minimal effect on the test results. The reason the NRMSE is small when the delay approaches a value even as large as 18msec. is due to the dominant wave load in the RTHS having the small frequency of 0.1Hz associated with the 10sec wave period. The measured restoring forces of the system does not undergo any significant change within the duration of 18msec. since the highest natural frequency observed to participate dynamically in the response during the RTHS is 0.697Hz.

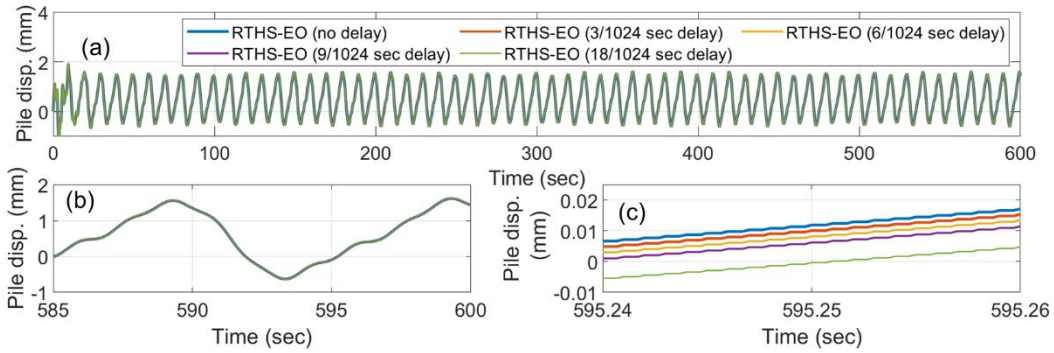

Figure 20: Pile head along-wind displacement time histories for various RTHS-EO with induced delay: (a) 0 to 600 seconds; zoomed in views for durations of (b) 585 to 600 seconds and (c) 595.24 to 595.26 seconds.

Table 3: NRMSE of along-wind pile head displacement for RTHS-EO with selected amounts of induced time delay

RTHS-EO	Induced Constant Time Delay (sec.)	NRMSE (%)
1	0	N/A
2	3/1024	0.058
3	6/1024	0.120
4	9/1024	0.185
5	18/1024	0.408

17. SUMMARY AND CONCLUSIONS

The real-time hybrid simulation (RTHS) concept is extended in this paper to offshore wind turbines (OWT) to enable the behavior of their pile foundation under realistic operational and more severe conditions to be studied. This paper presents the formulation of the RTHS framework. The framework includes the use of an unconditionally stable explicit integration algorithm to solve the equations of motion, a model with a transition substructure to enforce compatibility and equilibrium at the interface between the OWT tower above the transition piece and the analytical substructure below the transition piece, avoiding numerical instability associated with the interaction between the integration algorithm and the hydrodynamic loads, and the use of the Windows Application Programming Interface (API) that utilizes memory mapped objects to create a fast communication protocol between OpenFAST and the simulation coordinator.

OpenFAST is used to determine the aerodynamic and hydrodynamic loads acting on the structure, while also modeling the dynamics of the electric power generator, gearbox, rotor, drivetrain, nacelle and the associated control system for these components. The OWT portion above the transition point is modeled analytically within OpenFAST, while the structure below the transition point is modeled analytically via the analytical substructure within the simulation coordinator, and the pile foundation (experimental substructure) is embedded in the soil box. The equations of motion involving the aerodynamic and hydrodynamic loading and the effects of the dynamics of the electric power generator, gearbox, rotor, drivetrain, nacelle and the associated

control system for these components from OpenFAST are numerically integrated and the resulting target displacements are imposed onto the analytical and experimental substructures for each time step.

The RTHS framework enables the coupled nonlinear behavior of both the analytical and experimental substructures to be captured. It enables investigating the long- and short-term behavior of OWT pile foundations in different geographical locations by mimicking the soil of concern in the soil box and loading demand on the OWT. The RTHS framework presented in this paper offers a realistic approach to investigate the behavior of pile foundations since the deformations imposed onto the pile foundation accounts for the coupled response of the foundation with the rest of the OWT structure.

RTHS of a 5 MW OWT subjected to operational and more severe conditions were performed. The results demonstrated that the framework enables RTHS of OWT to be performed with pile foundations residing in a soil box. To achieve this success, solutions to several computational challenges associated with extending RTHS to OWT were developed. The study led to the following accomplishments and conclusions:

1. Partitioning of the equations of motion at the interface between the OWT model and the analytical substructure of the RTHS along with the use of a transition substructure is required to enable OpenFAST to perform its iteration procedure to determine the aerodynamic forces acting on the model and account for the effects of the dynamics of the electric power generator, gearbox, rotor, drivetrain, nacelle and the associated control system for these components;
2. To ensure stability of the integration of the equations of motion, the added hydrodynamic mass of the analytical substructure and the linearized hydrodynamic damping from the drag forces in Morison's equation needs to be moved to the left-hand side of the equations of motion when

computing the model integration parameters of the MKR-α method. During a RTHS the latter resides on the right hand side of the equations of motion. Linearization of the viscous drag term is based on the standard deviation of the relative velocity of the peak structural and fluid particles;

3. Creating memory mapped files enables a fast communication protocol to be established to exchange information between the RTHS coordinator and OpenFAST;
4. Suppression of the transient response at the start of the RTHS when using OpenFAST is necessary to avoid accumulating excessive damage to the pile foundation.

The RTHS framework for testing OWT systems is applicable to larger systems compared to the 5 MW OWT used herein as the prototype structure. For wet sand that has a rate dependency in its restoring force, researchers who consider using this framework will need to use a suitable modeling scale factor size, where the associated compressed time axis and the resulting model's time step size can be accommodated by the actuation, data acquisition, and simulation coordinator computer system's clock speeds.

18. ACKNOWLEDGEMENTS

The material presented herein is based upon work supported by the U.S. Department of Energy's Office of Energy Efficiency and Renewable Energy (EERE) Wind Energy Technologies Office under award number DE-EE0008964. Additional support is provided by Pennsylvania Infrastructure Technology Alliance (PITA) and MTS Corporation. Acknowledgements are extended to Professor Arindam Banerjee and Professor Justin Jaworski, as well to Kevin Wyckoff, Liam Magaral, and Sudharsan Kalidoss who are collaborators and provided advice on the hydrodynamic and aerodynamic loading aspects and modeling of OWT operational dynamics using OpenFAST. The technical support from ATLSS staff is greatly acknowledged. Any

opinions, findings, and conclusions expressed in this paper are those of the authors and do not necessarily reflect the views of the sponsors or others acknowledged herein.

19. REFERENCES

[1] Mahin S, Shing PS. Pseudodynamic method for seismic testing. J of Struct Engr 1985;111(7):1482-503.

[2] Nakashima M, Kato H, Takaoka E. Development of real- time pseudo dynamic testing. Earth Engr & Struct Dyn 1992;21(1):79-92. https://doi.org/10.1002/eqe.4290210106

[3] Kolay C, Al-Subaihawi S, Marullo T, Ricles, J, Quiel S. Multi-hazard real-time hybrid simulation of a tall building with damped outriggers. Int J of Lifecycle Perf Engr 2020;4(1-3):103-32. https://doi.org/10.1504/IJLCPE.2020.108937

[4] Al-Subaihawi S, Kolay C, Marullo T, Ricles J, Quiel S. Assessment of wind-induced vibration mitigation in a tall building with damped outriggers using real-time hybrid simulations. Engr Struct 2020;205:110044. https://doi.org/10.1016/j.engstruct.2019.110044

[5] Al-Subaihawi S, Marullo T, Ricles J, Quiel S. Multi-directional seismic behavior assessment of a tall building using real-time hybrid simulations. Proceedings of the 12th National Conference on Earthquake Engineering; 2022 June 27 – July 1; Salt Lake City, Utah, United States.

[6] Al-Subaihawi S, Ricles J, Quiel S. Online explicit model updating of nonlinear viscous dampers for real time hybrid simulation. Soil Dyn & Earth Engr 2022;154:107108. https://doi.org/10.1016/j.soildyn.2021.107108

[7] Dong B, Sause R, Ricles J. Accurate real- time hybrid earthquake simulations on large- scale MDOF steel structure with nonlinear viscous dampers. Earth Engr & Struct Dyn 2015;44(12):2035-55. https://doi.org/10.1002/eqe.2572

[8] Dong B, Sause R, Ricles J. Seismic response and performance of a steel MRF building with nonlinear viscous dampers under DBE and MCE. J of Struct Engr 2016;142(6):04016023. http://dx.doi.org/10.1061/(ASCE)ST.1943-541X.0001482

[9] Kolay C, Ricles J, Marullo T, Mahvashmohammadi A, Sause R. Implementation and application of the unconditionally stable explicit parametrically dissipative KR- α method for real- time hybrid simulation. Earth Engr & Struct Dyn 2015;44(5):735-55. https://doi.org/10.1002/eqe.2484

[10] Chen C, Ricles J, Marullo T, Mercan O. Real- time hybrid testing using the unconditionally stable explicit CR integration algorithm. Earth Engr & Struct Dyn 2009;38(1):23-44. https://doi.org/10.1002/eqe.838

[11] Karavasilis T, Ricles J, Sause R, Chen C. Experimental evaluation of the seismic performance of steel MRFs with compressed elastomer dampers using large-scale real-time hybrid simulation. Engr Struct 2011;33(6):1859-69. https://doi.org/10.1016/j.engstruct.2011.01.032

[12] Chen C, Ricles J. Large- scale real- time hybrid simulation involving multiple experimental substructures and adaptive actuator delay compensation. Earth Engr & Struct Dyn 2012;41(3):549-69. https://doi.org/10.1002/eqe.1144

[13] Chae Y, Ricles J, Sause R. Large-scale experimental studies of structural control algorithms for structures with magnetorheological dampers using real-time hybrid simulation. J of Struct Engr 2013;139(7):1215-26. http://dx.doi.org/10.1061/(ASCE)ST.1943-541X.0000691

[14] Covarrubias Vargas B, Harvey Jr, P, Cao L, Ricles J, Al- Subaihawi S, Villalobos Vega E. Characterization and real- time hybrid simulation testing of rolling pendulum isolation bearings with different surface treatments. Earth Engr & Struct Dyn 2022;51(11):2668-89. https://doi.org/10.1002/eqe.3694

[15] FACT SHEET: Biden Administration Jumpstarts Offshore Wind Energy Projects to Create Jobs. The White House 2021 March [cited 2023 April 12]. Available from: URL: https://www.whitehouse.gov/briefing-room/statements-releases/2021/03/29/fact-sheet-biden-administration-jumpstarts-offshore-wind-energy-projects-to-create-jobs/

[16] FACT SHEET: Biden- Harris Administration Announces New Actions to Expand U.S. Offshore Wind Energy. The White House 2022 September [cited 2023 April 12]. Available from: URL: https://www.whitehouse.gov/briefing-room/statements-releases/2022/09/15/fact-sheet-biden-harris-administration-announces-new-actions-to-expand-u-s-offshore-wind-energy/

[17] Jensen F, Falzon B, Ankersen J, Stang H. Structural testing and numerical simulation of a 34 m composite wind turbine blade. Comp struct 2006;76(1-2):52-61. https://doi.org/10.1016/j.compstruct.2006.06.008

[18] Bottasso C, Campagnolo F, Petrović V. Wind tunnel testing of scaled wind turbine models: Beyond aerodynamics. J of Wind Engr and Indus Aero 2014;127:11-28. https://doi.org/10.1016/j.jweia.2014.01.009

[19] Ushiyama I, Shimota T, Miura Y. An experimental study of the two-staged wind turbines. Ren Ener 1996;9(1-4):909-12. https://doi.org/10.1016/0960-1481(96)88427-8

[20] Wang X, Li S, Li J. Effect of pile arrangement on lateral response of group-pile foundation for offshore wind turbines in sand. App Ocean Res 2022;124:103194. https://doi.org/10.1016/j.apor.2022.103194

[21] Frick D, Achmus M. An experimental study on the parameters affecting the cyclic lateral response of monopiles for offshore wind turbines in sand. Soil and Foun 2020;60(6):1570-87. https://doi.org/10.1016/j.sandf.2020.10.004

[22] Cox J, O'Loughlin C, Cassidy M, Bhattacharya S, Gaudin C, Bienen B. Centrifuge study on the cyclic performance of caissons in sand. Int J of Phy Mod in Geo 2014;14(4):99-115. https://doi.org/10.1680/ijpmg.14.00016

[23] Su D, Wu W, Du Z, Yan W. Cyclic degradation of a multidirectionally laterally loaded rigid single pile model in compacted clay. J of Geo & Geoe Engr 2014;140(5):06014002. http://dx.doi.org/10.1061/(ASCE)GT.1943-5606.0001084

[24] Buchner B, Wichers J, De Wilde J. Features of the state-of-the-art deepwater offshore basin. Paper presented at the Offshore Technology Conference; 1999 May 3; Texas, United States. https://doi.org/10.4043/10814-MS

[25] Chabaud V, Steen S, Skjetne R. Real-time hybrid testing for marine structures: challenges and strategies. Proceedings of the ASME 2013 32nd International Conference on Ocean, Offshore and Arctic Engineering. Volume 5: Ocean Engineering; 2013 June 9–14; Nantes, France. https://doi.org/10.1115/OMAE2013-10277

[26] Sun C, Song W, Jahangiri V. A real-time hybrid simulation framework for floating offshore wind turbines. Ocean Engr 2022;265:112529. https://doi.org/10.1016/j.oceaneng.2022.112529

[27] Sadraddin H, Shao X. State-of-the-art of experimental methods for floating wind turbines. J of Ren and Sust Ener 2022;14(3):032701. https://doi.org/10.1063/5.0071943

[28] Song W, Sun C, Zuo Y, Jahangiri V, Lu Y, Han Q. Conceptual study of a real-time hybrid simulation framework for monopile offshore wind turbines under wind and wave loads. Front in Bld Envi 2020;6. https://doi.org/10.3389/fbuil.2020.00129

[29] Chabaud V, Eliassen L, Thys M, Sauder T. Multiple-degree-of-freedom actuation of rotor loads in model testing of floating wind turbines using cable-driven parallel robots. J Phy: Conf Ser 2018;1104:012021. DOI 10.1088/1742-6596/1104/1/012021

[30] Thys M, Chabaud V, Sauder T, Eliassen L, Sæther L, Magnussen Ø. Real-time hybrid model testing of a semi-submersible 10MW floating wind turbine and advances in the test method. Proceedings of the ASME 2018 1st International Offshore Wind Technical Conference. ASME 2018 1st International Offshore Wind Technical Conference; 2018 November 4–7; San Francisco, California, USA. https://doi.org/10.1115/IOWTC2018-1081

[31] Kanner S, Koukina E, Yeung R. Power optimization of model-scale floating wind turbines using real-time hybrid testing with autonomous actuation and control. J of Offsh Mech & Arc Engr 2019; 141(3): 031902. https://doi.org/10.1115/1.4041995

[32] Vilsen S, Sauder T, Sørensen A, Føre M. Method for real-time hybrid model testing of ocean structures: case study on horizontal mooring systems. Ocean Engr 2019;172:46-58. https://doi.org/10.1016/j.oceaneng.2018.10.042

[33] Vittori F, Azcona J, Eguinoa I, Pires O, Rodríguez A, Morató Á, Garrido C, Desmond C. Model tests of a 10 MW semi-submersible floating wind turbine under waves and wind using hybrid method to integrate the rotor thrust and moments. Wind Ener Sci 2022;7(5):2149-61. https://doi.org/10.5194/wes-7-2149-2022

[34] Bayati I, Facchinetti A, Fontanella A, Taruffi F, Belloli M. Analysis of FOWT dynamics in 2-DOF hybrid HIL wind tunnel experiments. Ocean Engr 2020;195:106717. https://doi.org/10.1016/j.oceaneng.2019.106717

[35] Belloli M, Bayati I, Facchinetti A, Fontanella A, Giberti H, La Mura, F, Taruffi F, Zasso A. A hybrid methodology for wind tunnel testing of floating offshore wind turbines. Ocean Engr 2020;210:107592. https://doi.org/10.1016/j.oceaneng.2020.107592

[36] Jonkman J, Musial W. Offshore code comparison collaboration (OC3) for IEA Wind Task 23 offshore wind technology and deployment. Golden (CO): National Renewable Energy Laboratory (US); 2010 Dec. Report No.: NREL/TP-5000-48191.

[37] Bergua R, Robertson A, Jonkman J, Branlard E, Fontanella A, Belloli M, et al. OC6 project phase III: validation of the aerodynamic loading on a wind turbine rotor undergoing large motion caused by a floating support structure. Wind Ener Sci 2023;8(4):465-85. https://doi.org/10.5194/wes-8-465-2023

[38] Popko W, Robertson A, Jonkman J, Wendt F, Thomas P, Müller K, et al. Validation of numerical models of the offshore wind turbine from the alpha ventus wind farm against full-scale measurements within OC5 Phase III. J of Offsh Mech and Arc Engr 2021;143(1): 012002. https://doi.org/10.1115/1.4047378

[39] Shaler K, Debnath M, Jonkman J. Validation of FAST.farm against full-scale turbine SCADA data for a small wind farm. J of Phy: Conf Ser 2020;1618:062061. DOI 10.1088/1742-6596/1618/6/062061

[40] Chopra A. Dynamics of structures: theory and applications to earthquake engineering. 3rd ed. Upper Saddle River (NJ): Prentice Hall Inc; 2007.

[41] Craig Jr, R, Bampton M. Coupling of substructures for dynamic analyses. AIAA J 1968;6(7):1313-19. https://doi.org/10.2514/3.4741

[42] Damiani R, Jonkman J, Hayman G. SubDyn user's guide and theory manual. Golden (CO): National Renewable Energy Laboratory (US); 2015 Sep. Report No.: NREL/TP-5000-63062.

[43] Jonkman J, Butterfield S, Musial W, Scott G. Definition of a 5-MW reference wind turbine for offshore system development. Golden (CO): National Renewable Energy Laboratory (US); 2009 Feb. Report No.: NREL/TP-500-38060.

[44] Jonkman J, Butterfield S, Passon P, Larsen T, Camp T, Nichols J, Azcona J, Martinez A. Offshore code comparison collaboration within IEA wind annex XXIII: phase II results regarding monopile foundation modeling. Golden (CO): National Renewable Energy Laboratory (US); 2008 Jan. Report No.: NREL/CP-500-42471.

[45] OpenFAST documentation. Release v3.1.0. National Renewable Energy Laboratory.

[46] Leishman J, Beddoes T. A semi- empirical model for dynamic stall. J of the Amer Helic Soc 1989;34:3-17. https://doi.org/10.4050/JAHS.34.3.3

[47] Moriarty P, Hansen A. AeroDyn theory manual. Golden (CO): National Renewable Energy Laboratory (US); 2005 Jan. Report No.: NREL/CP-500-36881.

[48] Jonkman J, Robertson A, Hayman G. HydroDyn user's guide and theory manual. Golden (CO): National Renewable Energy Laboratory (US).

[49] Morison J, Johnson J, Schaaf S. The force exerted by surface waves on piles. J of Petro Tech 1950;189:149-54. https://doi.org/10.2118/950149-G

[50] Journée JMJ, Massie WW. Offshore hydromechanics. 1st ed. Delft University of Technology; 2001.

[51] Bai Q, Bai Y. Subsea pipeline design, analysis, and installation. Gulf Professional Publishing; 2014.

[52] Moncarz P, Krawinkler H. Theory and application of experimental model analysis in earthquake engineering. Stanford (CA): John A. Blume Earthquake Engineering Center; 1981 Jun. Report No.: 50. http://purl.stanford.edu/rm315dh3494

[53] Altaee A, Fellenius B. Physical modeling in sand. Canadian Geo J 1994; 31(3): 420-31. https://doi.org/10.1139/t94-049

[54] LeBlanc C, Houlsby G, Byrne B. Response of stiff piles in sand to long-term cyclic lateral loading. Géotechnique 2010;60(2):79-90. https://doi.org/10.1680/geot.7.00196

[55] Klinkvort R, Hededal O. Effect of load eccentricity and stress level on monopile support for offshore wind turbines. Canadian Geo J 2014;51(9):966-74. https://doi.org/10.1139/cgj-2013-0475

[56] Bayton S, Black J, Klinkvort R. Centrifuge modelling of long term cyclic lateral loading on monopiles. Physical Modelling in Geotechnics [volume 1]. 1st ed. CRS Press; 2018: pp 689-694.

[57] The MathWorks Inc. MATLAB [computer program]. Version: 9.13.0 (R2022b). Natick (MA); 2022.

[58] Carrion J, Spencer B. Model-based strategies for real-time hybrid testing. Newmark Structural Engineering Laboratory, University of Illinois at Urbana-Champaign, 2007 Dec. Report No.: NSEL-006.

[59] Gasmi A, Sprague M, Jonkman J, Jones W. Numerical stability and accuracy of temporally coupled multi-physics modules in wind turbine CAE tools. Proceedings of the 51st AIAA Aerospace Sciences Meeting including the New Horizons Forum and Aerospace Exposition. 2013 Jan 7-10; Dallas, Texas, USA. https://doi.org/10.2514/6.2013-203

[60] Bashforth F, Adams JC. An attempt to test the theories of capillary action by comparing the theoretical and measured forms of drops of fluid. University Press; 1883.

[61] Moulton F. New methods in exterior ballistics. 1st ed. University of Chicago Press; 1926.

[62] Kolay C, Ricles J. Improved explicit integration algorithms for structural dynamic analysis with unconditional stability and controllable numerical dissipation. J of Earth Engr 2019;23(5):771-92. https://doi.org/10.1080/13632469.2017.1326423

[63] Aasen S, Page A, Skjolden Skau K, Nygaard,T. Effect of foundation modelling on the fatigue lifetime of a monopile-based offshore wind turbine. Wind Ener Sci 2017;2(2):361-76. https://doi.org/10.5194/wes-2-361-2017

[64] Kolay C. Parametrically dissipative explicit direct integration algorithms for computational and experimental structural dynamics [dissertation]. Bethlehem (PA): Lehigh Univ.; 2016.

[65] Housseine O, Monroy C, Bigot F. A new linearization method for vectorial Morison equation. Proceedings of the 30th International Workshop on Water Waves and Floating Bodies; 2015 April 12-15; Bristol, U.K.

[66] Wolfram J. On alternative approaches to linearization and Morison's equation for wave forces. Proceedings of the Royal Society of London. Series A: Mathematical, Physical and Engineering Sciences; 1999;455(1988):2957-74. https://doi.org/10.1098/rspa.1999.0434.

[67] Malhotra S. Design & construction considerations for offshore wind turbine foundations in north America. Civil Engr Practice J 2009; 24(1):7-42.

[68] Microsoft Corporation. Interprocess Communications 2021 July [cited 2023 April 12]. Available from: URL: https://learn.microsoft.com/en-us/windows/win32/ipc/interprocess-communications.

[69] Intel® Corporation. Intel® Fortran Compiler [cited 2023 April 12]. Available from: URL: https://www.intel.com/content/www/us/en/developer/tools/oneapi/fortran-compiler.html.

[70] Shi, S., Zhai, E., Xu, C., Iqbal, K., Sun, Y., and Wang S. Influence of Pile-Soil Interaction on Dynamic Properties and Response of Offshore Wind Turbine with Monopile Foundation in Sand Site. Journal of Applied Ocean Research. 2022; 126, 103279. https://doi.org/10.1016/j.apor.2022.103279

[71] Matha, D. Model development and loads analysis of an offshore wind turbine on a tension leg platform, with a comparison to other floating turbine concepts. Golden (CO): National Renewable Energy Laboratory (US); 2010 Feb. Report No.: NREL/SR-500-45891.

20. Appendix A – Listing and Values of Parameters

Table A.1: Parameter List

Parameter Description	Symbol	Value
Actuator controller sampling rate	f_{SA}	1024 Hz
Analytical defined foundation stiffnesses	k_y, $k_{\theta x}$, and $k_{\theta y}$	2.5e+6kN/m, 2.6E+8kN/rad, and 2.6E+8kN/rad
Blade-pitch rate limit	B_{PR}	8 deg
Blade model damping	ξ_B	0.47%
Cut-in & Cut-off wind speeds	v_{CIW}, v_{COW}	3, 25 m/sec
Drag coefficient	C_d	1.0
Drivetrain gearbox ratio	DT_g	97:1
Drivetrain rated rotor speed	DT_r	12 rpm
Drivetrain generator speed	DT_g	1174 rpm
Electric generator inertia	I_G	534 tons.m^2
Equivalent stiffness & damping coefficient scale factor	μ	0.5 – 2 (see Table 1)
Experimental substructure pile diameter	D_{ES}	0.05 m
Experimental substructure pile thickness	t_{ES}	2 mm
Experimental substructure equivalent stiffness	$k_{eq}\ (\omega)$	92.5kN/m
Experimental substructure equivalent damping coeff	$c_{eq}\ (\omega)$	5.02kN-sec/m, 4.83kN-sec/m
Experimental substructure scale factor	α	120
Gearbox equivalent damping dashpot	$c_{eq,GB}$	6.2 MN.m.s/rad
Gearbox equivalent stiffness	$K_{eq,GB}$	867 MN.m/rad
Gravitational constant	g	9.81m/sec^2
Hub rotational inertia	I_{HT}	115 tons.m^2
Hub translational inertia	I_{HT}	56 tons
Inertia coefficient	C_M	2.0
MKR-α algorithm high frequency spectral radius	ρ_∞	0.75
Nacelle rotational mass	$m_{N,\theta}$	2670 tons.m^2
Nacelle translation mass	$m_{N,}$	240 tons
Nacelle-yaw actuator rotation dashpot	$C_{NY,\theta}$	19 MN.m.s/rad
Nacelle-yaw actuator rotation spring	$K_{NY,\theta}$	9 GN.m/rad
OpenFAST 1st region minimum generator speed	$v_{GS,1}$	670rpm
OpenFAST last region minimum generator speed	$v_{GS,last}$	1173.7rpm
Prototype monopile height	H_M	66 m
Prototype monopile diameter	D_M	6 m
Prototype monopile segments	L_{AW}, L_S, L_E	10, 20, 36 m
Prototype rotor radius	R_r	90 m
Prototype steel monopile thickness	t_M	0.06 m
Prototype tapered tower diameter	D_{Tt}	6 – 3.87 m
Prototype tapered tower thickness	t_T	0.019 – 0.027 m
RTHS experimental scale factor	α	120
RTHS integration algorithm time step	Δt	3/1024 sec.
Soil box sand density	γ_s	1630 kg/m^3
Soil box sand internal friction angle	ϕ_s	35 deg
Soil model mean stress-to-prototype mean stress ratio	N	1
Time duration for20% supplemental damping	t_{Tr}	120 sec.
Tower model damping	ξ_T	1.0%
Wave period	T	10 sec.
Wave height	H	6, 12 m (see Table 1)
Wind speed	v_W	12, 20 m/sec (see Table 1)
Water density	γ_w	9.81kN/m^3